МІНІСТЕРСТВО ОСВІТИ І НАУКИ УКРАЇНИ
ДВНЗ «УЖГОРОДСЬКИЙ НАЦІОНАЛЬНИЙ УНІВЕРСИТЕТ»

НАУКОВИЙ ВІСНИК
УЖГОРОДСЬКОГО УНІВЕРСИТЕТУ

СЕРІЯ
«ФІЗИКА»

Науковий журнал

Випуск 52
2022

УЖГОРОД
2022

ISSN 2415-8038

Засновником журналу Науковий вісник Ужгородського університету. Серія «Фізика» є
ДВНЗ «Ужгородський національний університет», фізичний факультет
та Закарпатське фізичне товариство

Рекомендовано до друку та поширення
через мережу Інтернет Вченою Радою
ДВНЗ «Ужгородський національний університет»
(протокол № 11 від 22 грудня 2022 р.)

Свідоцтво про державну реєстрацію
друкованого засобу масової інформації
Серія КВ № 7972 від 09 жовтня 2003 р.

Журнал входить до переліку наукових фахових видань України
Категорія: Б. Науки: фізико-математичні. Спеціальності: 104 – Фізика та астрономія,
105 – Прикладна фізика та наноматеріали
(наказ Міністерства освіти і науки України від 11 липня 2019 р. № 975)

Журнал представлено у міжнародних наукометричних базах даних, репозитаріях та пошукових системах: Google Scholar, BASE, НБУ ім. В. І. Вернадського, Crossref, Scopus, OpenAIRE, WorldCat

Науковий вісник Ужгородського університету. Серія «Фізика» : наук. журн. / [редкол.: В. М. Різак (голов. ред.) та ін.]. – Ужгород : ДВНЗ «УжНУ», 2022. – Вип. 52. – 57 с.

Адреса редакції:
ДВНЗ «Ужгородський національний університет»
88000, вул. Університетська, 14, м. Ужгород
Закарпатська область, Україна
тел/факс: (03122) 3-20-24
E-mail: info@physics.uz.ua
www: https://physics.uz.ua/uk

MINISTRY OF EDUCATION AND SCIENCE
OF UKRAINE UZHHOROD NATIONAL UNIVERSITY

SCIENTIFIC HERALD
OF UZHHOROD UNIVERSITY

SERIES
“PHYSICS”

Scientific Journal

Issue 52
2022

UZHHOROD
2022

ISSN 2415-8038

The journal Scientific Herald of Uzhhorod University. Series “Physics” is founded
by Faculty of Physics, Uzhhorod National University
and Transcarpathian Physical Society

Recommended for printing and distribution
via the Internet by the Academic Council
of Uzhhorod National University
(Minutes No. 11 of December 22, 2022)

Certificate of state registration
of the print media
Series KV No. 7972 of October 09, 2003

The journal is included in the list of scientific professional publications of Ukraine
Category: B. Branch of Sciences: Physics and Mathematics. Specialties: 104 – Physics
and Astronomy, 105 – Applied Physics and Nanomaterials
(order of the Ministry of Education and Science of Ukraine of July 11, 2019 No. 975)

The journal is presented international scientometric databases, repositories
and scientific systems: Google Scholar, BASE, VNLU, Crossref, Scopus, OpenAIRE, WorldCat

Rizak V.M., et al. Scientific Herald of Uzhhorod University. Series “Physics”. Issue 52. Uzhhorod: Uzhhorod National University; 2022. 57 p.

The address of editorial board:
Uzhhorod National University
88000, 14 Universytetska Str., Uzhhorod
Transcarpathian region, Ukraine
Tel./fax: (03122) 3-20-24
E-mail: info@physics.uz.ua
www: https://physics.uz.ua/en

НАУКОВИЙ ВІСНИК УЖГОРОДСЬКОГО УНІВЕРСИТЕТУ.
СЕРІЯ «ФІЗИКА»
ВИПУСК 52

Редакційна колегія

SCIENTIFIC HERALD OF UZHHOROD UNIVERSITY.
SERIES "PHYSICS"
ISSUE 52

Editorial Board

ЗМІСТ

SCIENTIFIC HERALD OF UZHHOROD UNIVERSITY.
SERIES “PHYSICS”
ISSUE 52

CONTENTS

Scientific Herald of Uzhhorod University
Series “Physics”

Journal homepage: https://physics.uz.ua/en
Issue 52, 9-15
Received: 08/30/2022. Revised: 10/12/2022. Accepted: 11/02/2022

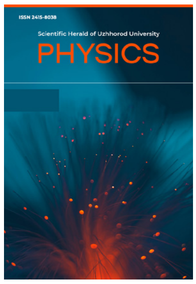

UDC: 536.2, 54-165.2
PACS: 72.15.Jf, 44.10.+i
DOI: 10.54919/2415-8038.2022.52.9-15

Thermal conductivity of solid solutions of $Bi_2(Te_{1-x}Se_x)_3$ (x = 0-0.07)

Kateryna Martynova[1*], Olena Rogacheva[2]

[1]ORCID: https://orcid.org/0000-0001-9739-4584.
National Technical University “Kharkiv Polytechnic Institute”,
61002, 2 Kyrpychova Str., Kharkiv, Ukraine

[2]Full Doctor of Physical and Mathematical Sciences, Professor.
ORCID: https://orcid.org/0000-0001-7584-656X.
National Technical University “Kharkiv Polytechnic Institute”,
61002, 2 Kyrpychova Str., Kharkiv, Ukraine

Abstract

Relevance. Solid solutions $Bi_2(Te_{1-x}Se_x)_3$ are effective materials for an *n*-leg of thermoelectric cooling devices. Recently, concentration anomalies of properties with a low impurity content were detected in these solid solutions ($x \sim 0.01$). It is important to establish whether similar anomalies would be observed on the dependence of thermal conductivity λ from the composition of the solid solution, since λ is one of the parameters that determine the thermoelectric quality factor of the material.

Purpose. The purpose of this study was to investigate the concentration dependences of the thermal conductivity of the solid solution of $Bi_2(Te_{1-x}Se_x)_3$ in the interval x = (0-0.07) to identify concentration anomalies and their possible impact on thermoelectric (TE) efficiency.

Methodology. Investigation of temperature dependences of thermal conductivity λ was performed by a dynamic calorimeter. Isotherms of λ for different temperatures in the range T = 175-400 K were built on their basis**.**

Results. On isotherms of λ, there is an interval of abnormal growth λ**,** which becomes more pronounced when the temperature decreases. The presence of this interval is associated with critical phenomena that accompany the transition of the percolation type from dilute to concentrated solid solutions.

Conclusions. The estimation of the thermoelectric figure of merit Z of materials is given. It is shown that the detected growth of λ leads to a decrease in Z in the ranges near the critical (x = 0.01), which should be considered in the practical use of solid solutions of $Bi_2(Te_{1-x}Se_x)_3$

Keywords: thermoelectric materials V_2VI_3, thermal properties, composition, percolation, thermoelectric figure of merit

Suggested Citation:
Martynova K, Rogacheva E. Thermal conductivity of solid solutions of $Bi_2(Te_{1-x}Se_x)_3$ (x = 0-0.07). *Scientific Herald of Uzhhorod University. Series “Physics”.* 2022;(52):9-15.

*Corresponding author

Introduction

It is known [1-3] that the efficiency of a thermoelectric (TE) material is largely determined by the value of its TE figure of merit ($Z=S^2\sigma/\lambda$, where S – Seebeck coefficient, σ – electrical conductivity, λ – thermal conductivity of the material). The most important task of materials science is to find ways to improve *Z*, including by a decrease in thermal conductivity [4; 5]. One of the conventional ways to increase *Z*, proposed in 1956 [6] – creation of solid solutions (SS) based on promising thermoelectrics.

Semiconductor alloys $Bi_2(Te_{1-x}Se_x)_3$ in the field of existence of solid solutions (x~0-0.2 and x~0.5-1, respectively [7; 8]), are known as effective materials for *n*-legs of TE cooling devices operating at temperatures near room temperature [1; 2; 9]. The maximum Z in these SS was obtained in the range of compositions x=0.07-0.2 (exact interval x depended on the technology of samples' manufacturing) [10-12].

Earlier in the study of concentration dependencies *S* and σ cast and cold-pressed samples of the system $Bi_2(Te_{1-x}Se_x)_3$, the authors of this study observed anomalies of properties near the composition $x = 0.01$, the presence of which was associated with the phase transition (PT) from diluted to concentrated solid solution [13]. Similar anomalies were observed earlier in [14] for a large number of solid solutions. Additional evidence in favour of this assumption was the discovery in [15] of a peak on the concentration dependence of heat capacity *C*. If such a PT occurs, it would certainly also affect the concentration dependence of λ, and, accordingly, the nature of the Z(x) dependence.

Thermal conductivity of solid solution of $Bi_2(Te_{1-x}Se_x)_3$ has been widely studied to date. Temperature dependencies λ of $Bi_2(Te_{1-x}Se_x)_3$ SS are given in a number of studies [16-18]. For SS of $Bi_2(Te_{1-x}Se_x)_3$ there are three components of thermal conductivity that influence the course of dependence λ(T): electronic, lattice, and bipolar thermal conductivity. The ratio of λ components of the material depends on the manufacturing technology, and on the heat and mechanical treatment of the sample. The transition to bipolar heat transfer with increasing temperature should be accompanied by an increase in λ. Currently, available data on the bipolar component of λ are somewhat contradictory. Thus, growth of λ at temperatures above T = 350 K was observed in pure Bi_2Te_3 in [16], and in SS of $Bi_2(Te_{1-x}Se_x)_3$ in monocrystalline samples in [18]. However, in the studies [17; 19] in composite samples of SS $Bi_2(Te_{1-x}Se_x)_3$ (x = 0-1) growth of λ was not observed.

Many studies have data of the dependence of λ on the composition of SS of $Bi_2(Te_{1-x}Se_x)_3$ x for monocrystalline [20; 21] and polycrystalline [19; 22] samples. According to this data, the dependency λ on the composition of the SS is a curve with two minima, between which there is a local maximum at x~0.33 [9]. In [20], it was shown that this composition of SS corresponds to the establishment of an ordered compound Bi_2Te_2Se.

To date, for $Bi_2(Te_{1-x}Se_x)_3$ SS there are no detailed studies of concentration dependence λ in the composition interval near pure Bi_2Te_3.The question arises: will the concentration dependencies of thermal conductivity reproduce the anomalies that the authors observed on the concentration dependencies σ and S in previous studies [13; 15]. The study of λ for small samples samples with small values of x would allow estimating the value of Z and drawing a conclusion about the influence of property anomalies on the TE figure of merit of SS of $Bi_2(Te_{1-x}Se_x)_3$.

The purpose of this study was to investigate the concentration dependences of the thermal conductivity of SS of $Bi_2(Te_{1-x}Se_x)_3$ in the interval x = (0-0.07) to identify concentration anomalies and their possible impact on thermoelectric efficiency.

Materials and Methods

Cold-pressed tablets (diameter d = 15 mm and height h = 5 mm) of $Bi_2(Te_{1-x}Se_x)_3$ ($0 \leq x \leq 0.07$) for measuring λ were made from annealed ingots of the solid solution of $Bi_2(Te_{1-x}Se_x)_3$ SS. For the production of ingots, a mixture of high-purity (99.999% of the main element) Bi, Se, and Te with the corresponding ratio of components was placed in quartz ampoules pumped to a pressure of ~10^{-3} Pa. The ampoules were heated in a furnace to ~1,200 K and kept at this temperature for 5-6 hours using vibration mixing. The samples were then annealed for 200 hours at 820 K, and then cooled to room temperature. The resulting ingots were ground into powder in an automated SBMM agate mortar. The resulting powder was sifted through a sieve (cell size 200 microns). The powder was pressed at room temperature on a hydraulic press (pressure P = 7 t/cm^2, exposure time under load – 1 min.). After manufacturing, the tablets were annealed in evacuated ampoules made of heat-resistant glass for 200 hours at a temperature of T = 575 K and cooled at the speed of the switched-off furnace.

Thermal conductivity measurements were performed on a dynamic calorimeter IT-λ-400 in the temperature range of 175 K – 625 K. Before installing the sample into the experimental cell, the contact surfaces were sanded to a mirror-like gloss and a thin layer of KPT-8 thermal paste was applied to them. After the sample was installed, the experimental cell was cooled with liquid nitrogen to a temperature of ~150 K. The study was conducted in the monotonous heating mode at a speed of ~0.1 K/s. The thermal conductivity was measured in temperature increments of 25 K. To control the reproducibility of the results, the λ value for each sample was taken twice. When the sample was re-installed in the cell, a layer of thermal paste was re-applied to the contact surfaces. Thus, the λ value for a sample of a certain composition, the data given in this paper represent the averaging of two measurements. Figure 1 shows the results of two measurements of λ for the sample Bi_2Te_3(points 1 and 2 correspond to separate experiments). It can be argued that the results of two experiments for the same sample actually coincide within the margin of error. The root-mean-square error did not exceed 5%.

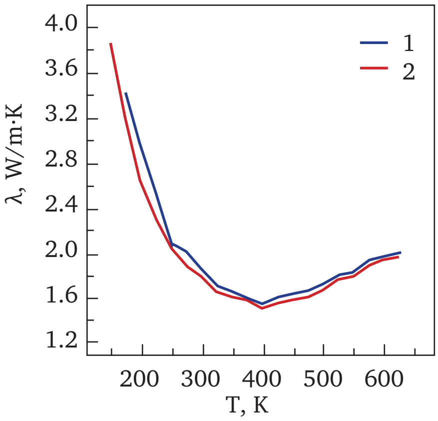

Figure 1. Experimental temperature dependences of thermal conductivity λ for a solution of Bi_2Te_3 (points 1 and 2 correspond to separate experiments)

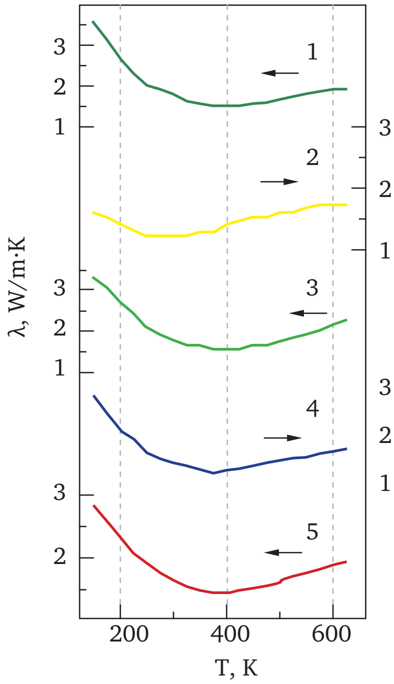

Figure 2. Temperature dependences of thermal conductivity λ for solid solutions of $Bi_2(Te_{1-x}Se_x)_3$ of different composition
(*1* – x = 0; *2* – x = 0.005; *3* – x = 0.0125; *4* – x = 0.02; *5* – x = 0.045)

Results and Discussion

Temperature dependences of thermal conductivity λ of cold-pressed and annealed SS of $Bi_2(Te_{1-x}Se_x)_3$ with different values of x are shown in Figure 2. You can see that for all samples λ first decreases in the temperature range T = 150 ÷ 350 K, after which at T=350÷625 K there is an increase in λ with increasing temperature. Such a course of dependence λ(T) indicates a change in the dominant heat transfer mechanism as the temperature increases.

Initial decline λ is associated with the fact that at temperatures below room temperature, heat transfer is provided by fluctuations in the crystal lattice (lattice thermal conductivity λ_L) and free electrons (electronic thermal conductivity λ_e). Both of these components decrease as the temperature increases, which leads to a decrease in the overall λ. Growth of λ at higher temperatures T~350 K can be explained by the fact that at these temperatures, the probability of heat transfer by electron-hole pairs increases (bipolar thermal conductivity λ_b) [16]. As noted above, such a course of temperature dependence of λ is typical for Bi_2Te_3 and SS on its basis, and was observed in [16; 18; 23]

Based on temperature dependencies λ, thermal conductivity isotherms for temperature values T = 175; 225; 300; 350, and 400 K were constructed (Fig. 3). For all temperatures, a general downward trend towards a decrease in λ with increasing x can be observed, which corresponds to the available literature data [19-21]. It is known that the development of SS of Bi_2Te_3 and Bi_2Se_3 significantly reduces the lattice component of thermal conductivity compared to pure initial compounds and the ordered phase of Bi_2Te_2Se. Analysis of the data provided in various studies shows that the data on the dependence of $\lambda_L(x)$, are successfully described by the Calloway-von Bayer-Clemens model for scattering in SS [9].

It can be seen that for all temperatures after the initial decrease in λ, an interval of increasing thermal conductivity is observed (x = 0.005-0.01), resulting in a peak in the dependence λ (x). With increasing temperature, the magnitude (height) of the peak, which characterises the degree of growth in λ, decreases, and at 400 K the peak becomes hardly noticeable.

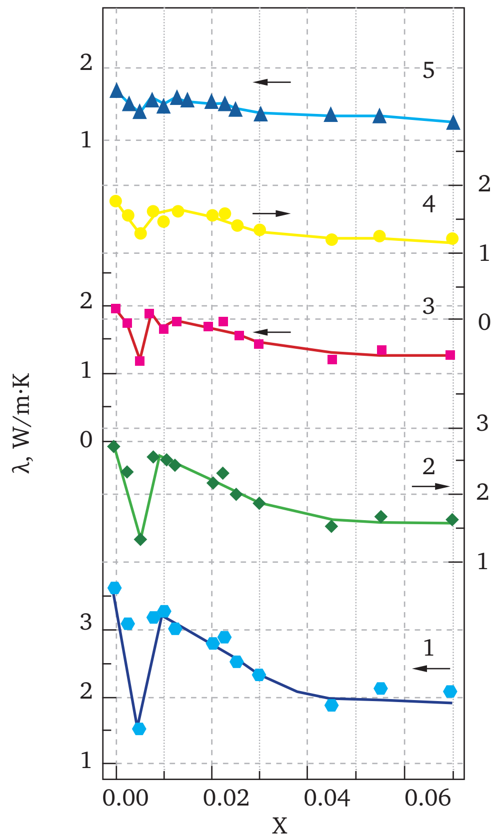

Figure 3. Thermal conductivity isotherms of λ of solid solutions of $Bi_2(Te_{1-x}Se_x)_3$ (*1* – *T* = 175 K; *2* – *T* = 225 K; *3* – *T* = 300 K; *4* – *T* = 350 K; *5* – *T* = 400 K)

Abnormal growth of λ in the interval x=0.005-0.01 is an additional evidence that in the specified range of compositions, transformations in the crystal are implemented during the formation of SS, which affect the processes of phonon scattering. As in previous studies [13], it is advisable to associate these transformations with the implementation of PT from diluted to concentrated solid solution. The likely mechanism for implementing these processes is described in detail in the review paper [14], which also provides a large number of experimental confirmations of this hypothesis. A more detailed description of these effects in relation to SS of $Bi_2(Te_{1-x}Se_x)_3$ is given in [13; 15].

These processes can be briefly described as follows. During isovalent substitution of Te→Se, a deformation sphere is formed around each impurity atom. Percolation theory, according to [24], states that there is a certain critical concentration of such spheres (the percolation threshold), at which they begin to interact collectively and a continuous chain of interactions (an infinite cluster) is created. Its development is a PT, the implementation of which results in anomalies in the dependencies of the properties of the SS on its composition. As in previous studies, the authors suggest calling solid solution diluted before reaching the threshold of percolation and the formation of an infinite cluster, and concentrated – after these processes have already passed.

Separately, it is worth noting that the growth of λ_L relative to neighbouring compounds at x = 0.033, which was observed in [19], may also be related to the proximity to a similar "percolation maximum" on dependency $\lambda_L(x)$.

In [13], the TE values of the parameters of cold-pressed and annealed samples $Bi_2(Te_{1-x}Se_x)_3$ were determined, namely, the electrical conductivity and Seebeck coefficient. Supplementing these data with the values of λ obtained in this study, the values of TE figure of merit Z for these SS at room temperature were calculated. The dependency Z(x) (Fig. 4a) also has a non-monotonic character: at the beginning of SS development, the figure of merit increases rapidly, reaching the value Z ~1.5 10^{-3} K^{-1} at x ~0.005. After that, in the interval x ~0.005-0.02 value Z decreases, after which there is an increase of Z up to x ~0.07.

Figure 4b shows the findings regarding dependency $Z(x)$ in comparison with the data of the studies [22] (hot-pressed samples) and [19] (composite samples). The Z values obtained in this study correspond to the data for samples made by other methods. The highest received value of Z corresponds to the composition x=0.07 and amounts to Z ~2.1 10^{-3} K^{-1} which within the error limit of the definition of Z coincides with the maximum value of Z, which was observed in [19] for composite materials.

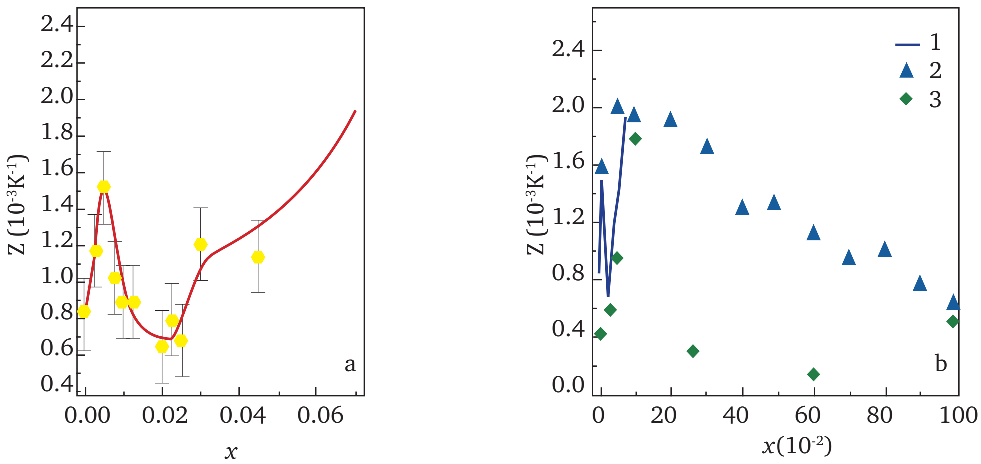

Figure 4. Dependence of thermoelectric figure of merit *Z,* which was calculated using the data from [13], on the composition of $Bi_2(Te_{1-x}Se_x)_3$ (x = 0-0.07) (a); Z(x) dependence obtained in this study, in comparison with the data of other researchers (*1* – this study, *2* –[22]; *3* – [19]) (b)

The results of this study, together with the results of [13], demonstrate that percolation PT affects all TE properties of SS of $Bi_2(Te_{1-x}Se_x)_3$, leading to an increase in electrical and thermal conductivity and a decrease in S in the area near x=0.01. But the effect of percolation PT on the TE figure of merit is determined by a combination of these parameters. In Figure 4b, the growth of λ in the proximity of percolation PT (x ~0.01) leads to a decrease in Z, compensating for growth σ, which was observed in [13] thus, SS has relatively high values of Z in the region befor PT (x = 0-0.005), and acquires maximum values in the region after PT (x ~ 0.07).

Conclusions

1. Temperature dependences (T = 175-600 K) of thermal conductivity λ of cold-pressed and annealed samples of solid solutions of $Bi_2(Te_{1-x}Se_x)_3$ in the interval of compositions (x = 0-0.07 are obtained and isotherms λ(x) are constructed on their basis.

2. All isotherms λ(x) revealed an interval (x = 0.005-0.01) of abnormal growth in λ, the presence of which is associated with critical phenomena that accompany the transition.

3. It is shown that at room temperature, an abnormal increase in thermal conductivity leads to a decrease in TE figure of merit Z in the range of compositions near the critical (x = 0.01). Maximum value of Z obtained in the region of concentrations under study corresponds to the composition x = 0.07 and is $Z = (2.1 \pm 0.2) \cdot 10^{-3}$ K^{-1}.

4. The detected concentration anomalies of TE properties accopanying the transition from dilute to concentrated solid solutions should be considered when interpreting experimental results and practical applications of solid solutions of $Bi_2(Te_{1-x}Se_x)_3$, and other solid solutions.

Further studies of this system would include the investigation of the temperature dependences of the Seebeck coefficient and electrical conductivity, and the construction of isotherms of these properties in the range of compositions (x = 0-0.07). This will reveal how the effect of concentration anomalies on the thermoelectric Q-factor of $Bi_2(Te_{1-x}Se_x)_3$ will change with a change in temperature.

References

[1] Uher C, editor. Materials aspect of thermoelectricity. Boca Raton: CRC Press; 2016. 624 p.

[2] Rowe DM, editor. Materials, preparation, and characterization in thermoelectric. Boca Raton: CRC Press; 2012. 552 p.

[3] Wei J, Yang L, Ma Z, Song P, Zhang M, Ma J, et al. Review of current high-ZT thermoelectric materials. *J. Mater. Sci.*, 2020;(55):article number 12642. doi: 10.1007/s10853-020-04949-0.

[4] Mukherjee M, Srivastava A, Singh AK. Recent advances in designing thermoelectric materials *J. Mater. Chem. C*, 2022;(10):12524-555. doi: 10.1039/D2TC02448A.

[5] Qin B, Wang D, Zhao L-D. Slowing down the heat in thermoelectrics. *InfoMat*. 2022(3(7)):755-89. doi: 10.1002/inf2.12217.

[6] Ioffe AF, Airapetyants SV, Ioffe AB, Kolomoets NV, Stilbans LS. On improving the efficiency of semiconductor thermocouples. *Dokl. AN SSSR*. 1956;(106):981-82.

[7] Sokolov OB, Skipidarov SY, Duvankov NI, Shabunina GG. Chemical reactions on the Bi_2Te_3-Bi_2Se_3 section in the process of crystal growth. *J. Cryst. Growth*. 2004;(262):442-48. doi: 10.1016/j.jcrysgro.2003.10.073.

[8] Chizhevskaya SN, Shelimova LE, Kosyakov VI, Shestakov VA. Critical evaluation and data reconciliation on the phase diagram of the Bi-Te-Se system and crystal structure of Bi_2Te_3-Bi_2Se_3 cut alloys. *Inorg. Mat.* 1997;(33(8)):903-11.

[9] Witting IT, Ricci F, Chasapis TC. The thermoelectric properties of n-type bismuth telluride: Bismuth selenide alloys $Bi_2Te_{3-x}Se_x$. *Research*, 2020;(1(15)):aticle number 4361703. doi: 10.34133/2020/4361703.

[10] Zhu T, Hu L, Zhao X. New insights into intrinsic point defects in V_2VI_3 thermoelectric materials. *Adv. Sci.* 2016;(3(16)):article number 1600004. doi: 10.1002/advs.201600004.

[11] Hu L, Zhu T, Liu X, Zhao X. Point defect engineering of high-performance bismuth-telluride-based thermoelectric materials. *Adv Funct Mater.* 2014;(24(33)):article number 5211-218. doi: 10.1002/adfm.201400474.

[12] Fang T, Li X, Hu C, Zhang Q, Yang J, Zhang W, Zhu T. Complex band structures and lattice dynamics of Bi2Te3 based compounds and solid solutions. *Adv Funct Mater.* 2019;(29(28)):article number 1900677. doi: 10.1002/adfm.201900677.

[13] Rogacheva EI, Martynova EV, Shelest TN, Doroshenko AN, Nashchekina ON. Percolation effects and self-organization processes in cold-pressed $Bi_2(Te_{1-x}Se_x)_3$ solid solutions. *Mater Today Proc.* 2020;(44):3506-510. doi:10.1016/j.matpr.2020.09.159.

[14] Rogacheva EI. Percolation effects and thermoelectric materials science. *J. Thermoelectr*. 2007;(2):61-72. doi: 10.1002/9781119407348.ch9.

[15] Martynova KV, Rogacheva EI, Lisachuk GV. Specific heat of $Bi_2(Te_{1-x}Se_x)_3$ solid solutions. *Func. Mat.* 2021;(28(4)):662-68.

[16] Goltsman BM, Kudinov VA, Smirnov IA. Semiconducting thermoelectric materials based on Bi_2Te_3. Moscow: Nauka; 1972. 320 p.

[17] Liu W, Lukas KC, McEnaney K, Lee S, Zhang Q, Opeil CP, et al. Studies on the Bi_2Te_3–Bi_2Se_3–Bi_2S_3 system for mid-temperature thermoelectric energy conversion. *Energy Environ Sci*. 2013;(6):552-60. doi: 10.1039/C2EE23549H.

[18] Prokofieva LV, Pshenay-Severin DA, Konstantinov PP, Shabaldin AA. Optimum composition of a $Bi_2Te_{3-x}Se_x$ alloy for the n-type leg of a thermoelectric generator. *Semiconductors.* 2009;(43(8)):973-76. doi: 10.1134/S1063782609080016.

[19] Soni A, Yanyuan Z, Ligen Y, Khor M, Aik K, Dresselhaus MS, et al. Enhanced thermoelectric properties of solution grown $Bi_2Te_{3-x}Se_x$ nanoplatelet composites. *Nano Lett.* 2012;(12):1203-209. doi: 10.1021/nl2034859.

[20] Birkholtz U. Untersuchung der intermetallischen Verbindung Bi_2Te_3 sowie der fasten Lösungen $Bi_{2-x}Sb_xTe_3$ und $Bi_{2-x}Te_xSe_3$ im Hinblick auf die Eignung als Materialien für Halbleiterthermoelemente. *Z. Naturforsch.* 1958;(13a):780-92.

[21] Goldsmid HJ. Recent studies of bismuth telluride and its alloys. *J. Appl. Phys.* 1961;(32): 2198-202. doi: 10.1063/1.1777042.

[22] Oh TS, Hyun DB, Kolomoets NV. Thermoelectric properties of the hot-pressed $(Bi,Sb)_2(Te,Se)_3$ alloys. *Scr Mater.* 2000;(42):849-54. doi: 10.1016/S1359-6462(00)00302-X.

[23] Qian D, Ye Z, Pan L, Zuo Z, Yang D, Yan Y. The mechanical and thermoelectric properties of Bi2Te3-Based alloy prepared by constrained hot compression technique. *Metals*. 2021;(11):article number 1060. doi: 10.3390/ met11071060.

[24] Stauffer D, Aharony A. Introduction to percolation theory. London/Washington DC: Taylor & Francis; 1992. 192 p.

Теплопровідність твердих розчинів $Bi_2(Te_{1-x}Se_x)_3$ (x = 0-0.07)

Катерина Вікторівна Мартинова[1], Олена Іванівна Рогачова[2]

[1]ORCID: https://orcid.org/0000-0001-9739-4584.
Національний технічний університет «Харківський політехнічний інститут»,
61002, вул. Кирпичова, 2, м. Харків, Україна

[2]Доктор фізико-математичних наук, професор. ORCID: https://orcid.org/0000-0001-7584-656X.
Національний технічний університет «Харківський політехнічний інститут»,
61002, вул. Кирпичова, 2, м. Харків, Україна

Анотація

Актуальність. Тверді розчини $Bi_2(Te_{1-x}Se_x)_3$ – це ефективні матеріали для *n*-гілки термоелектричних охолоджуючих пристроїв. Нещодавно в цих твердих розчинах були виявлені концентраційні аномалії властивостей за малого вмісту домішки ($x \sim 0.01$). Важливо встановити, чи будуть аналогічні аномалії спостерігатися на залежності теплопровідності λ від складу твердого розчину, оскільки λ є одним із параметрів, що визначає термоелектричну добротність матеріалу.

Мета. Метою цієї роботи було дослідження концентраційних залежностей теплопровідності ТР $Bi_2(Te_{1-x}Se_x)_3$ в інтервалі x = (0-0.07) для виявлення концентраційних аномалій та їх можливого впливу на ТЕ ефективність.

Методологія. Дослідження температурних залежностей теплопровідності λ проводили методом динамічного калориметра. На їх основі побудовані ізотерми λ для різних температур в інтервалі T = 175-400 К.

Результати. На ізотермах λ спостерігається інтервал аномального зростання λ, яке стає більш вираженим при зниженні температури. Наявність цього інтервалу пов›язується з критичними явищами, що супроводжують перехід перколяційного типу від розведених до концентрованих твердих розчинів.

Висновки. Надана оцінка термоелектричної добротності Z матеріалів. Показано, що виявлене зростання λ призводить до зменшення Z в інтервалі складів поблизу критичного (x = 0.01), що необхідно враховувати при практичному застосуванні твердих розчинів $Bi_2(Te_{1-x}Se_x)_3$

Ключові слова: термоелектричні матеріали V_2VI_3, теплові властивості, склад, перколяція, термоелектрична добротність

Scientific Herald of Uzhhorod University
Series "Physics"

Journal homepage: https://physics.uz.ua/en
Issue 52, 16-26
Received: 09/15/2022. Revised: 10/28/2022. Accepted: 11/17/2022

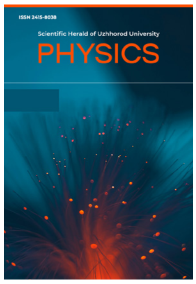

UDC 539.1.09, 658.562: 621
PACS 29.17.+w, 29.27._a
DOI: 10.54919/2415-8038.2022.52.16-26

Optimal scheme for stimulating photofission of shielded nuclear materials on the Microtron M-30: a combination of theoretical and experimental studies

Igor Pylypchynets*

Postgraduate Student, ORCID: https://orcid.org/0000-0002-0120-7703.
Institute of Electron Physics of the NAS of Ukraine,
88017, 21 Universitetska Str., Uzhhorod, Ukraine

Abstract

Relevance. The photofission of shielded nuclear materials is widely used to develop methods for non-destructive analysis of their isotopic composition. To stimulate the photofission reaction, bremsstrahlung beams obtained on electronic accelerators are used. Their parameters significantly depend on the design features of accelerators and sample activation schemes.

Purpose. Theoretical modelling of parameters of an optimal scheme for stimulating the photofission of shielded nuclear materials on an electronic accelerator – Microtron M-30 for the analysis of their isotopic composition, considering its technical characteristics, and experimental verification of its parameters.

Methodology. Theoretical calculations of the parameters of bremsstrahlung beams for the Microtron M-30 were carried out using the GEANT4 toolkit. For experimental studies of the influence of structural elements of the optimal stimulation scheme on the integral characteristics of inhibitory photons, secondary photoneutrons, the method of activation of detectors made of gold was used; for residual electrons – the transmission method based on a passage chamber and a Faraday cylinder.

Results. As a result of the combination of theoretical and experimental studies, optimal parameters of the activation scheme of nuclear materials on the Microtron M-30 have been established. The scheme provides experimental conditions under which the losses of bremsstrahlung photon beams interacting with the test samples (with energies ≥6 MeV) do not exceed 35% of their initial values, with the practical absence of residual electrons (98% of electrons are absorbed) and secondary photoneutrons (no more than 1E-9 n/e).

Conclusions. The parameters of the developed stimulation scheme for the Microtron M-30 can be applied to various types of accelerators, considering their design features, characteristics of the samples, and implemented activation schemes

Keywords: bremsstrahlung, residual electrons, secondary photoneutrons, GEANT4, activation detector, Faraday cylinder

Suggested Citation:
Pylypchynets I. Optimal scheme for stimulating photofission of shielded nuclear materials on the Microtron M-30: a combination of theoretical and experimental studies. *Scientific Herald of Uzhhorod University. Series "Physics"*. 2022;(52):16-26.

*Corresponding author

Introduction

Control of the circulation and non-proliferation of nuclear materials (e.g. fertile – ^{232}Th, ^{238}U; divisible – ^{235}U, ^{239}Pu) is one of the most urgent tasks of nuclear science and technology [1]. Reliable information about their isotopic composition is required to successfully solve this problem. One of the methods for analysing the isotopic composition of nuclear materials, which is widely used and improved (developed) at the present time, is based on the use of information about gamma and neutron radiation from their decay products formed as a result of the photofission reaction [2-4]. As a rule, sealed containers made of stainless steel are used for the storage and transportation of nuclear materials [5; 6]. To stimulate the photofission of shielded nuclear materials, bremsstrahlung beams obtained at electronic accelerators (linear, microtrons) are widely used [1; 3; 5]. For efficient use of bremsstrahlung beams in the analysis, it is necessary that their energy is higher than the thresholds (γ,f) of reactions for nuclear materials, and less than the thresholds of possible photonuclear reactions that can occur (be generated) in the container material [7].

The outputs of bremsstrahlung photons and their energy spectra obtained by converting electron beams into bremsstrahlung (via the (e,γ) reaction channel) depend primarily on the initial electron energy, characteristics (material, geometric dimensions) of converters [8-10]. The electron spans in the materials from which the converters are made will be greater than the thickness at which the photon outputs have maximum values, i.e., residual electrons will be present in the beams [11].

Residual electrons, when interacting with the studied samples, can generate secondary photons [12] and photoneutrons in them (via (e,n) reaction channels) [13; 14]. The generation of secondary photons and photoneutrons is also possible when they interact with stainless steel screens (the material from which containers for nuclear materials are made) [15]. In this regard, there is a need to "clean" the bremsstrahlung beams from residual electrons and photoneutrons, since their presence can significantly affect the final results of the analysis. To reduce the number of residual electrons interacting with the studied samples, without significantly weakening the intensity of bremsstrahlung photons, filters are used – materials with a small charge number. Boron carbide (B_4C) as a material for the manufacture of filters meets these criteria (absorbs residual electrons, secondary photoneutrons without significant deformation of the photon spectrum) [16; 17].

Notably, the quantitative (integral) content of photons, residual electrons and secondary photoneutrons and their ratios in the bremsstrahlung beams interacting with the studied samples of shielded nuclear materials are significantly influenced by geometric factors (the relative position of the converter, the studied sample relative to the axis of the initial electron beam), and the presence of additional structural elements (filters, screens, collimators) used in their generation [19]. In addition, the final parameters of the bremsstrahlung beams will be affected by the design features of devices (nodes) for the output of electron beams into the air, which differ significantly for different types of electronic accelerators [20]. Therefore, these factors should be considered when developing sample activation schemes.

To obtain information about the characteristics of bremsstrahlung beams that interact with the studied samples obtained on electronic accelerators, considering their design features and irradiation schemes, computer modelling is widely used using Monte Carlo programme codes (MCNP6, FLUKA, GEANT4) [21; 22], since experimental studies (for example: activation, track detectors, TLD dosimeters, proportional counters) require expensive and long-term measurements [23; 24].

Purpose of the study: development of an optimal stimulation scheme (generation of bremsstrahlung beams with the maximum content of photons with energies above the thresholds of the photofission reaction with the minimum content of residual electrons and secondary photoneutrons) of the photofission of shielded nuclear materials on the electronic accelerator of the Institute of electronic physics of the National Academy of Sciences (IEP NAS) of Ukraine – Microtron M-30, considering its technical characteristics, for the needs of analysing their isotopic composition, and experimental verification of its parameters.

Materials and Methods

Modelling of parameters of bremsstrahlung beams for the Microtron M-30 electronic accelerator using GEANT4 toolkit

To simulate the spectra of photons, residual electrons, and secondary photoneutrons that fall into the plane of location (installation) of test samples (or on the samples themselves) perpendicular to the beam axis of the primary electrons, and their angular distribution (which allowed visualising their profile images in the plane along the x and y axes perpendicular to the z axis), a C++ programme was developed using the GEANT4 class library [25]. The choice of this toolkit was conditioned by its suitability for modelling the processes of generation of various types of particles and their interaction with the studied samples at electronic accelerators [1; 10; 21], and its availability in terms of free use. The programme provided for the possibility of considering the primary parameters: electron beams (initial geometric dimensions (point source, parallel beam) and beam distribution (Gauss, equally probable)); the presence of converters (converters of electrons to photons) and filters for its generation; samples (particle detectors), and considering their location in three-dimensional space, which allowed reproducing the real irradiation schemes of the samples implemented on electronic accelerators (in this case, on the electronic accelerator of the IEP of the National Academy of Sciences of Ukraine – Microtron M-30 [26]).

The programme was implemented under the Windows platform using multi-threading mode. A computer with a 6-core Intel(R) Core(TM) i7-9750H (2.60 GHz) processor and 36 GB of RAM was used for calculations.

Calculations were performed at the initial electron energies of 12.5 MeV [7] for the geometric dimensions of the output beam, which had the shape of an ellipse with axes of 22×6 mm [27].

Figure 1 shows a scheme for stimulating the photofission reaction of shielded nuclear materials on the Microtron M-30, where 1 – Microtron M-30 output node; 2 – Ti window; 3 – photon converter ((Ta, 52×45×(0.1÷4 mm); 4 – filter B_4C (diameter – 30 mm, thickness – 19 mm); 5 – stainless steel screen (diameter = 23 mm, thickness = 0.1÷9.5 mm); 6 – sample of nuclear material.

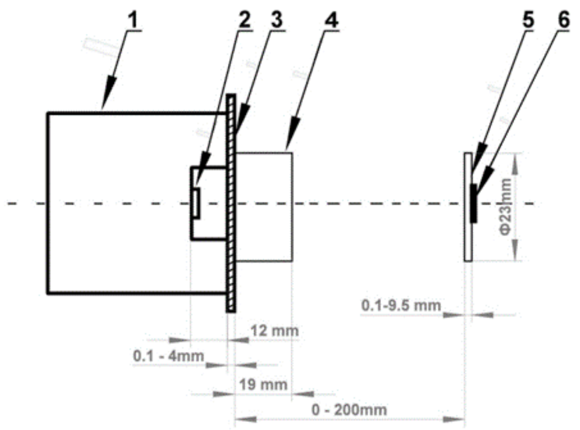

Figure 1. Scheme for stimulating the photofission reaction of shielded nuclear materials on the Microtron M-30

In all calculations, an equally probable distribution of initial electrons along the plane was set (considering the design features of the electron output unit – a titanium window with a thickness of 0.05 mm) [27]. Distance from the output node to the tantalum (Ta) converter (dimensions: 52×45×T mm [T=0.1; 0.5; 1.0; 1.5; 2.0; 3.0; 4.0 mm]) was 12 mm. The test sample (nuclear material; radius – 5.6 mm) was fixed perpendicular to the beam axis at a distance of 0; 25; 50; 75; 100; 125; 150; 175; 200 mm from Ta of the converter. Additionally, the influence of the presence of structural materials (B4C filter (diameter – 30 mm, length – 19 mm) [16], stainless steel screen (0÷9.5 mm)) in schemes for stimulating the photofission of nuclear materials to the final characteristics of bremsstrahlung (the ratio of photons, residual electrons, photoneutrons) was studied. The relative absorption coefficients of photons and electrons (A) were determined by the equation

$$A = (1- I/I_0)\cdot 100\ \% \qquad (1)$$

where I and I_0 – integral values of particle fluxes (photons or electrons) that interact with the sample after passing through the layer with the absorbing material and in its absence.

Experimental studies of the influence of structural elements of the photofission stimulation scheme on the parameters of bremsstrahlung beams

Experimental studies of the effect of a combination of structural elements (Ta converter, B_4C filter, stainless steel screen) of schemes for stimulating the photofission of nuclear materials to the final parameters of bremsstrahlung beams (the ratio of photons, residual electrons, secondary photoneutrons) interacting with the samples under study were performed by the transmission method [27; 28]. During the experiment, integral values of photon fluxes and relative absorption coefficients of photons and electrons for a combination of structural elements were determined.

Photons and photoneutrons. For experimental determination of the integral characteristics of photons and photoneutrons in bremsstrahlung beams interacting with the sample, and their relative absorption coefficients for a combination of structural materials (B_4C filter (diameter – 30 mm, length – 19 mm) + stainless steel screen (diameter – 34 mm, thickness – 9.5 mm)) activation detectors containing gold isotope – ^{197}Au were used [24; 28; 29]. The geometric dimensions of the activation detectors (square shape, rib length – 6.6 mm) were close to the size of the samples of nuclear materials in terms of area. Photons (for the energy interval – 8.1÷12.5 MeV) and photoneutrons were determined by activation products ^{197}Au by channels of (γ,n)- reactions: ^{196}Au (gamma energy of the line Eγ = 355.7 KeV, its quantum output Iγ=87%, reaction threshold – 8.01 MeV) and for (n,γ)- reactions: ^{198}Au (Eγ = 411.8 KeV, Iγ = 95.6%) [30], respectively. The relative photon absorption coefficients were determined by the ratios of the gamma radiation intensity from the detector activation products ^{197}Au, irradiated with and without structural materials. The exposure time of the detectors was 15 minutes. Measurements of gamma radiation from generated radionuclides ^{196}Au and ^{198}Au was performed on the ORTEC spectrometric complex [28] for 200 hours. The measurement time of activation detectors was 25 minutes. At least 10 series of measurements were performed for each individual detector. The statistical error of spectrometric measurements did not exceed 3%. The measured intensity values were normalised to the integral values of the primary electron flow, the area of activation detectors, and the number of isotope nuclei of ^{197}Au contained in the detectors.

Electrons. Experimental determination of relative values of electron absorption coefficients separately for structural materials (Ta converter (thickness – 1 mm), B_4C filter (diameter – 30 mm, length – 19 mm), stainless steel screen (diameter – 34 mm, thickness – 9.5 mm)) and their combinations (Ta converter + B_4C + stainless steel), which were used to form photon beams to stimulate the photofission reaction of nuclear materials, were performed by the transmission method described in detail in [27; 28]. Measurements of the integral flow of electrons from the window of the accelerator output unit and the layers of structural materials that passed through and their combinations were carried out using a secondary emission monitor (pass-through chamber) and a Faraday cylinder, respectively. Electron detection was carried out in the plane of placement of the test samples.

Results and Discussion

As a result of the calculations, the dependences of the spectra of photons, residual electrons, and secondary photoneutrons (which were used to determine their integral characteristics and relations between them) interacting with the test sample on the thickness of the inhibitory target – tantalum (Ta) converter (0.1÷4.0 mm) and the distance from Ta converter to the test target (0÷200 mm) were studied. Figures 2 and 3 show the dependences of the spectra of photons and residual electrons normalised to one electron (1e) on the thickness of Ta converter at a fixed distance Ta converter – test sample = 100 mm, respectively.

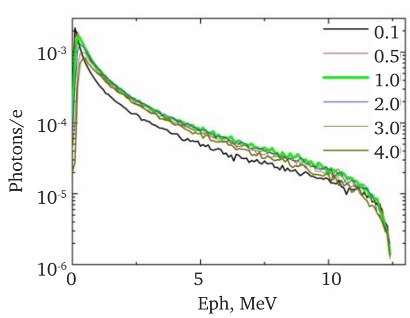

Figure 2. Dependences of bremsstrahlung photon spectra on Ta converter thickness

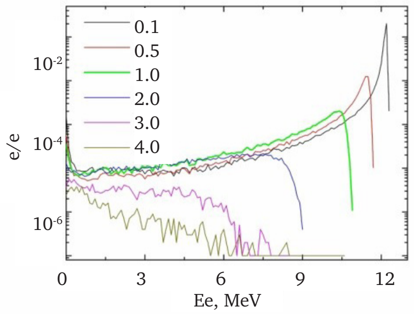

Figure 3. Dependences of residual electron spectra on Ta converter thickness

The relationship between the integral values of photon yields in the low-energy (with energies <6 MeV, which do not affect the sample activation process) and high-energy (with energies from 6 to 12.5 MeV, which stimulate the actinide photofission) parts of the spectra on the thickness of the inhibitory target is established. As the Ta converter thickness increase to ~1.0 mm, the values of the total integral photon outputs increase and reach a maximum value of – 2.11E-2, with a further increase in thickness to 4 mm, the values are constant. For photons with energies ≥6 MeV, the optimal thickness is 1 mm (1.92 E-3). The relationship between the integral values of secondary electron fluxes (which did not participate in the generation of bremsstrahlung photons) in the low-energy (with energies <6 MeV) and high-energy (with energies between 6 and 12.5 MeV, which can generate secondary photons when interacting with the sample) parts of the spectra also depends on the thickness of the Ta tconverter. As the Ta converter thickness increase from 0.1 to 4 mm, the values of the integral fluxes of residual electrons (with energies <6 MeV) decrease from 3.77E-2 to 3.3E-6, respectively. With a thickness of 1 mm, it amounts to 3.36E-3.

Dependences of the spectra of bremsstrahlung photons and residual electrons (normalised to 1e) entering the sample on the distance Ta converter – sample (0÷200 mm) with a fixed thickness of the Ta converter = 1 mm are shown in Figures 4 and Figure 5, respectively. The relations between the integral values of photon fluxes and secondary electrons in the low- and high-energy parts of the spectra depend on the distance. As it increases from 0 to 200 mm, the values of Integral photon fluxes and residual electrons (with energies <6 MeV) decrease from 4.21E-2 to 6.69E-4, and from 3.26E-2 to 8.24E-5, respectively.

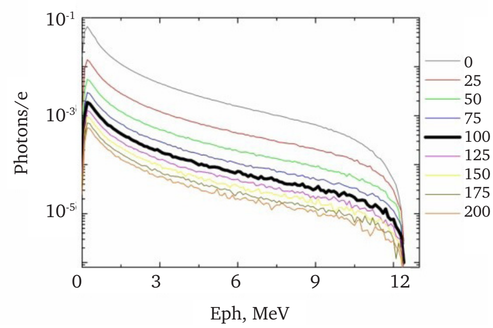

Figure 4. Dependences of bremsstrahlung photon spectra on distance Ta converter – sample

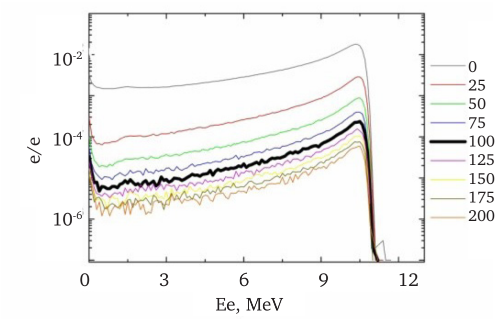

Figure 5. Dependences of residual electron spectra on distance Ta converter – sample

Figure 6 shows the spectrum of secondary photoneutrons generated by the interaction of electrons with Ta converter (normalised to 1e). The numerical value of the integral photoneutron flux is normalised to 1e – 9.3E-6. The integral value of the photoneutron flux interacting with the test sample did not exceed – 1E-8 photoneutrons per 1e, which is consistent with the calculation results in [9; 13].

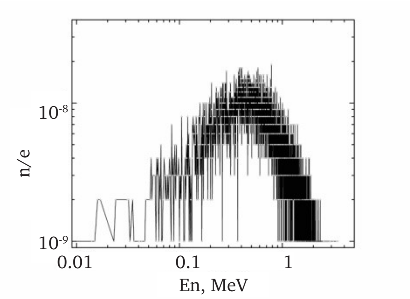

Figure 6. Energy spectrum of photoneutrons

The obtained results reproduce the general patterns that are characteristic of the dependence of photon outputs on the thickness of converters and the influence of geometric factors on the activation process and are consistent with existing data [9; 10; 13], and their difference is associated with the use of different input parameters during simulations [19; 20], which indicates the need to take them into account.

The calculations established the value of the optimal thickness of Ta converter, at which the integral output of the generated photons (in the beam of bremsstrahlung) is the maximum, and the distance Ta converter – test sample, which provides the best ratio between photons, residual electrons, and secondary photoneutrons interacting with the sample (the maximum integral value of the photon flux at the minimum values of electrons, photoneutrons). The optimal thickness of the Ta converter is 1 mm at a fixed distance Ta converter – sample installation plane is 100 mm. Integral values of photon fluxes and residual electrons with energies ≥6 MeV (normalised to 1e) are – 1.92 E-3 and – 3.36E-3, respectively. These values for photons and electrons are 19.9 and 98.5 times less than the zero distance (when the sample is placed close to the converter). A further increase in the distance from 100 mm to 200 mm reduces the value of integral electron fluxes by only 4.0 times.

Notably, when using such a sample activation scheme, additional purification of the bremsstrahlung beam from residual electrons is necessary [16; 28]. Therefore, calculations were made for the absorption of bremsstrahlung photons and residual electrons by a filter made of B_4C [16]. Figures 7 and 8 show the spectra of photons and residual electrons (normalised to 1e) interacting with the test sample in the presence of B_4C filter and its absence for a fixed distance from Ta converter (thickness – 1 mm) – test sample = 100 mm, respectively. It is established for the first time that the total number of electrons and photons absorbed by a B_4C filter – 79.64% and 14.7%, respectively, with energies ≥6 MeV – 99.8% and 9.3%.

The obtained results reflect the general regularities of the relative absorption coefficients of photons and electrons (for the energy region – 6.5÷12.5 MeV) by a conventionally used filter (reactor graphite) in the generation of bremsstrahlung photon beams to stimulate photonuclear reactions [28]. However, for B_4C filter, the values of the electron absorption coefficients are higher and the photons are less than those of reactor graphite, which confirms the effectiveness of its use for stimulation schemes.

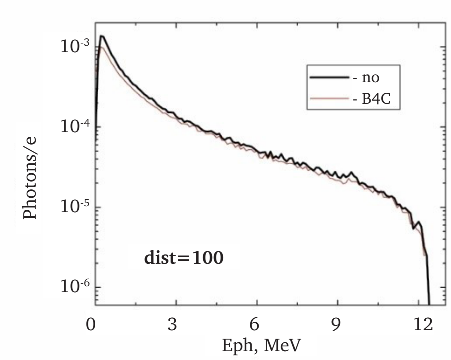

Figure 7. Spectra of photons interacting with the sample without and with B_4C filter.

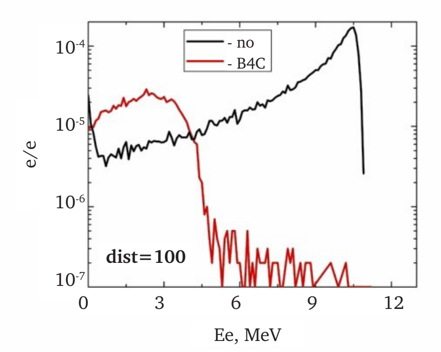

Figure 8. Spectra of electrons interacting with the sample without and with B_4C filter

Additionally, simulations of the influence of the thickness (0.1, 0.5, 1.0, 3.0, 5.0, 7.0, 9.5 mm) of the stainless steel screen on the final parameters of the bremsstrahlung beam (photons, residual electrons) interacting with the sample were carried out. Figures 9 and 10 show the dependences of the spectra of photons and residual electrons interacting with samples at a fixed distance Ta converter (thickness – 1 mm) – test sample = 100 mm, on the thickness of the stainless steel screen.

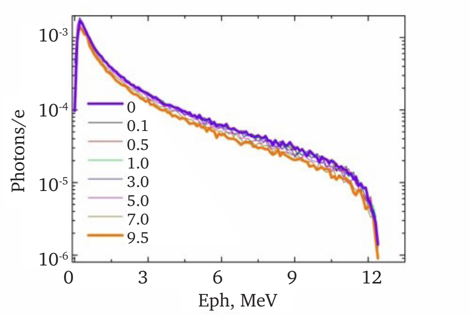

Figure 9. Dependences of the spectra of photons interacting with samples on the thickness of the stainless steel screen

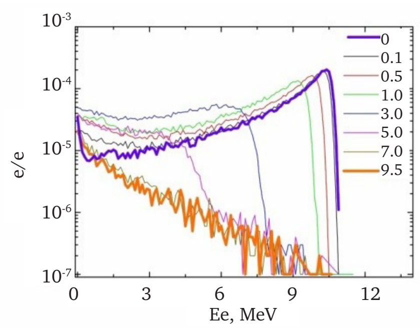

Figure 10. Dependences of the spectra of residual electrons interacting with samples on the thickness of the stainless steel screen

Values of the relative absorption coefficients (according to equation 1) of photons and electrons with energies ≥6 MeV, depending on the screen thickness, are shown in Figure 11. For the first time, it was found that when the screen thickness is more than 5 mm, 99% of electrons and 15% of photons are absorbed. With a further increase in the screen thickness to 9.5 mm, 28% of photons are absorbed.

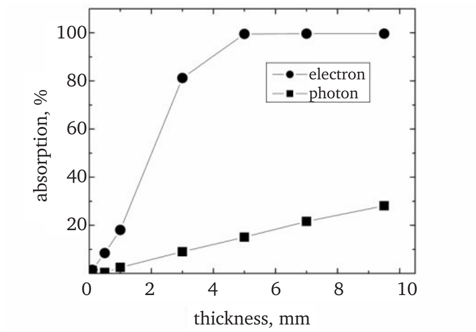

Figure 11. Dependence of photon and electron absorption (with energies ≥6 MeV) on the thickness of the stainless steel screen

The calculations were used as input data for modelling the parameters of the optimal scheme for stimulating the photofission of nuclear materials on the Microtron M-30, considering the technical features of its electron output unit and the characteristics of samples. The activation scheme for shielded (thickness – 9.5 mm – samples of nuclear materials consists of Ta converter (thickness – 1 mm) and B_4C filter. The distance from Ta converter to the test sample – 100 mm. The influence of the structural elements of the activation scheme on the final shape of the spectra of photons and residual electrons that fall on the samples was investigated (Figures 12 and 13, respectively).

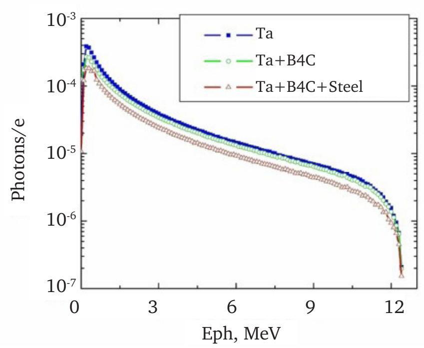

Figure 12. Spectra of photons interacting with samples for optimal stimulation scheme

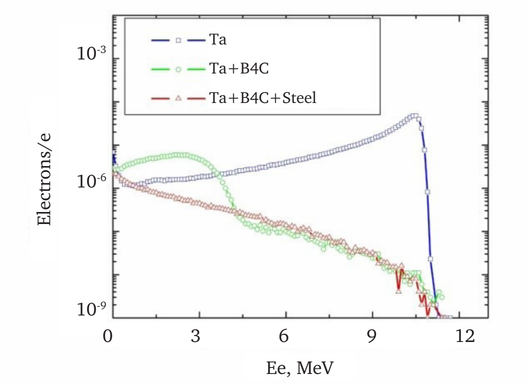

Figure 13. Spectra of residual electrons interacting with samples for optimal stimulation scheme

The integral values of photon fluxes, residual electrons normalised to one electron, falling on samples of shielded nuclear materials are – 2.87E-3 photons (with an energy >6 MeV – 2.86E-4) and 3.89E-5 electrons (with an energy >6 MeV – 2.454E-6). When performing calculations based on a given activation scheme, photoneutrons that fell on samples of shielded nuclear materials were not detected.

For the proposed scheme of stimulating the photofission, 7.87E-1% of photons and 1.48E-2% of electrons from their total number (those that fall into the plane of sample placement) fall on the samples. Similarly, they interact with samples (energies >6 MeV) – 1.09% of photons and 1.08E-3% of electrons, respectively.

Thus, the presented scheme allows almost completely excluding the interaction of residual electrons and secondary photoneutrons with the studied samples of shielded nuclear materials, that is, excluding the stimulation of additional channels of electro-nuclear ((e,γ)-, (e,n)-, (e,f)-) and neutron ((n,γ)-, (n,f)-) reactions [7], which may introduce additional errors in the final results of the analysis of their isotopic composition.

Comparison with the experiment

Photons. Value of integral photon beam fluxes (normalised to 1e), interacting with samples of nuclear materials, without structural elements (straight beam) and when combined with B_4C filter + stainless steel screen was 4.63E-5 and 3.08E-5, respectively. The obtained values are consistent with the results of calculations using the GEANT4 toolkit (4.32E-5 and 2.896E-5) within 6.69% and 5.97%.

Results of measurements of the dependence of the relative intensity values (which were used to determine the photon absorption coefficient) of gamma-rays of the generated radionuclide ^{196}Au from its cooling time are shown in Figure 14. Experimental values of gamma intensity of activation detectors for a direct beam of photons hitting the sample were circles, combinations of filter + steel screen – squares. The results of theoretical calculations [28] for identical experimental conditions (at the same activation, cooling, and measurement times) are represented by solid lines. The experimental values are consistent with the calculation results within 5%. The total measurement error did not exceed 10%. The main contribution to the error was made by the uncertainty of the number of isotope nuclei ^{196}Au, and was ~7%.

The error of the obtained experimental values can be further influenced by the factor associated with the process of irradiation of gold samples, namely, with the instability of the efficiency of the output of the primary electron beam from the microtron output node during their activation. Even with stable operation of the microtron, the output efficiency can vary from 85 to 90%, since it depends on the process of focusing the electron beam in the centre of the Ti window [26-28].

Photon absorption coefficient value for the combination B_4C filter + steel screen was – 33.3%, which was consistent with the calculation result of the GEANT4 toolkit (36.34%) within 9.1%.

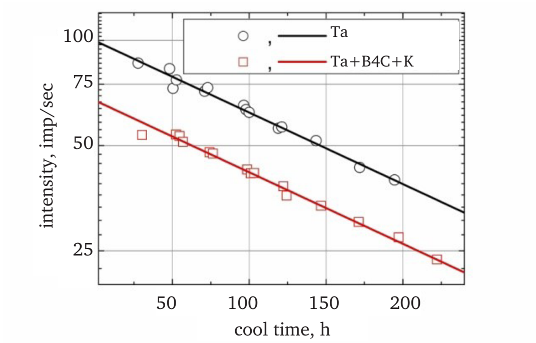

Figure 14. Dependences of the relative intensity of gamma radiation of a radionuclide ^{196}Au on cooling time

Photoneutrons. When performing spectrometric measurements of irradiated gold detectors placed in the plane of installation of test samples, lines from isotopes ^{198}Au, generated along the channel (n,γ)- reactions, the measured gamma-ray spectra are absent (within the background), and their value is less than the detection limit. This indicates the absence of photoneutrons in the bremsstrahlung beam interacting with test samples, which is consistent with the results of the calculations performed.

Electrons. Values of electron absorption coefficients for combinations Ta converter + B_4C filter, Ta converter + B_4C filter + steel – 83.74% and 98%, and are consistent with the results of calculations with GEANT4 toolkit (79.64% and 95.46%) in the range of 4.9% and 2.6%, respectively.

The results of experimental studies of the parameters of bremsstrahlung beams and the effect of structural elements of the activation scheme on their characteristics confirm the results of calculations performed using the GEANT4 toolkit.

A significant discrepancy between theoretical calculations and experimental results is associated with errors in nuclear data used in GEANT4 toolkit libraries [21; 25], affecting modelling accuracy.

The obtained results complement the existing information on the methods of generating bremsstrahlung beams with specified parameters on electronic accelerators to stimulate the photofission of nuclear materials as unshielded – ^{235}U, ^{238}U, ^{239}Pu [2]; ^{235}U, ^{238}U [3]; ^{235}U, ^{238}U, ^{239}Pu [4], and shielded, packed in stainless steel containers, – ^{232}Th [5]; ^{238}U, ^{239}Pu (additional studies were conducted for the case of a carbon steel container) [6].

These papers present the results of both theoretical calculations performed using Monte Carlo codes: MCNP6 [2] and a combination of PHITS 3/0 and MCNP6 [3] for initial electron energies of 8 and 7, and 13.5 MeV, respectively, and experimental studies conducted on linear accelerators for a wide energy range from 7 to 17.5 MeV (7 and 9 [6]; 10 [5] and 17.5 [4]) at average peak electron currents on bremsstrahlung converters from 30 mA [5] to 100 mA [4; 6]. Metal plates of tantalum (Ta) with a thickness of 0.5 mm [3] and 2 mm [5] and tungsten (W) with a thickness of 5 mm [4] and 1.8 mm [6] were used as converters for generating bremsstrahlung.

Notably, the numerical values of the electron flux currents generated by microtrons are an order of magnitude less than on linear accelerators due to differences in their principle of operation [1]. Therefore, this factor must be considered when developing schemes for stimulating the photofission of nuclear materials for conducting the procedure for their isotope identification.

Cylindrical lead (Pb) collimators were used to focus them on the studied samples of shielded [6] and unshielded [4] nuclear materials during their activation. The need for their use was conditioned by the use of schemes for online detection of gamma and neutron radiation from the decay products of nuclear materials, during the procedure for their isotope identification. Since detectors require protection (the geometric dimensions of which must be cons when placing the studied samples when activating them) from the parasitic background of bremsstrahlung photons and neutrons formed during the operation of linear accelerators [5]. However, their use leads to a weakening of the bremsstrahlung beams and their additional contamination with photoneutrons [19]. In contrast, in [5], during the activation of samples, an uncollimated beam of bremsstrahlung was used, which provided more efficient use of the initial electron flux.

Monte Carlo codes were used to model the characteristics of the bremsstrahlung photon spectra obtained at linear electron accelerators: FLUKA [5] MCNP6 [4; 6]. Only in [4], experimental studies of the characteristics of bremsstrahlung photon fluxes at a maximum energy of 17.5 MeV were conducted using activation detectors made of Au (Gold), Ni (nickel), U (uranium), Zn (zinc), and Zr (zirconium).

When electrons (Ee=7÷10 MeV [3; 5; 6]) interact with Ta [3; 5] and W [6] converters, the fluxes of secondary photoneutrons generated through the channels of electro and photonuclear reactions [9; 13] did not affect the final results of the analysis of the isotopic composition of nuclear materials.

In the case of interaction of electrons (Ee=17.5 MeV) with a W converter with a thickness of 5 mm [4], the resulting secondary photoneutrons can additionally initiate channels of neutron fission reactions (n,f) of nuclear materials, since their cross-sections (for the energy region of fast neutrons, which are the main components of the energy spectra of photoneutrons [9]) are approximately several times larger than the cross-sections of photofission reactions [31], which can affect the accuracy of the analysis of their isotopic composition. Therefore, when activating samples of nuclear materials on a linear accelerator [4], a combined filter was used to purify the bremsstrahlung beam from the photoneutrons present in it, generated by the interaction of electrons (Ee=17.5 MeV) with the W converter and additionally generated by interaction with the Pb collimator. The filter consisted of layers of boron polyethylene (thickness – 200 mm) and cadmium (thickness – 2 mm), which allowed almost completely protecting test samples from interaction with photoneutrons [4].

In the above studies on the use of photofission stimulation schemes for unshielded [2; 3; 4] and shielded [5; 6] nuclear materials, the interaction of residual electrons with the samples under study was not analysed.

The most important indicator of the effective use of activation schemes of nuclear materials in the analysis of their isotopic and quantitative composition is information on the numerical values of the outputs of photofission reactions ((number of acts of photofission)/(1e)·(gram)), which occurred during their stimulation by beams of bremsstrahlung on electronic accelerators [7]. The percentage of occurrence of photofission acts (i.e., the number of photons and neutrons generated from the decay products of nuclear materials used in the analysis process [2; 3; 4]) affects the lower weight limit of their identification.

As a result of the analysis of the yield dependence ((number of photofission acts)/(1e) * (gram)) of the photofission reaction of the ^{238}U nucleus from the energy of electrons (which, when interacting with the inhibitory target, generate high-energy photons), it was found that the numerical values of the yield change by about 4 orders of magnitude for the energy region from ~6 (reaction threshold) to ~20 MeV, and for the energy region ~(6÷13) MeV – by more than 3 orders of magnitude [7]. Therefore, a further increase in the energy of accelerated electrons leads to a change in the yield by less than an order of magnitude.

The number of photofission acts of nuclear materials depends on the energy and quantitative parameters (fluxes per second) of bremsstrahlung beams obtained at electronic accelerators, the nuclear and physical characteristics of the samples under study, since it directly depends on the cross-sections of photofission [1; 31], and on their weight.

The weights of the test samples used in the process of stimulating the photofission of nuclear materials for unshielded samples were: 1.5 g – ^{235}U, 2.1 g – ^{238}U, 0.47 g – ^{239}Pu [2]; 1.9 g – ^{235}U + ^{238}U [3]; 1.0÷1e+2 g – ^{235}U, 1e+2÷1e + 3 g – ^{238}U, 1.0 g – ^{239}Pu [4]; for shielded samples: 15.6 g – ^{232}Th [5]; 241 G – ^{238}U [6]. Their use allowed obtaining statistically accurate and reliable results when analysing the isotopic composition.

When performing the procedure for identifying nuclear materials directly in stainless steel containers, it is necessary to consider the attenuation of photons and neutrons generated during photofission when passing through a steel container. The solution to this problem is achieved by increasing the weight of the studied samples and the current strength of electronic flows generated by accelerators.

The proposed stimulation scheme allows more efficient use of the initial electron beam (the number of photons with energies ≥6 MeV interacting with the sample formed at 1e) to stimulate the photofission of shielded nuclear materials, i.e., reduces the cost of the analysis procedure.

Conclusions

The use of a combination of theoretical and experimental studies establishes optimal parameters of the scheme for stimulating the photofission of shielded nuclear materials on an electronic accelerator – Microtron M-30 for analysing their isotopic composition. Namely, to obtain the information necessary for the generation of bremsstrahlung beams with the maximum photon content with the minimum (or practically absent) content of residual electrons, secondary photoneutrons interacting with test samples, with mandatory consideration of their characteristics, design features of the Microtron M-30, and the activation scheme. This approach can be used to develop schemes for photonuclear activation analysis of the isotopic composition of special materials for various types of electronic accelerators.

The conducted studies allow predicting the sensitivity of the method for identifying nuclear materials depending on the strength of electron beam currents during sample irradiation. And, for the first time, the established values of the relative absorption coefficients of photons and electrons with energies ≥6 MeV, depending on the thickness of the stainless steel screen, allow adjusting the parameters of the photofission schemes of nuclear materials in containers of arbitrary geometric shape.

For the first time, the values of the relative absorption coefficients of photons and electrons with energies ≥6 MeV were established by filters made of B_4C, allow developing more efficient schemes for generating bremsstrahlung photon beams to stimulate photonuclear reactions compared to conventionally used filters.

This approach can be used to develop schemes for photonuclear activation analysis of the isotopic composition of special materials for various types of electronic accelerators.

Funding

The work was partially carried out within the framework of the project of research works of young scientists of the National Academy of Sciences of Ukraine in 2021-2022. State registration number – 0121U111832).

References

[1] Zilges A, Balabanski DL, Isaak J, Pietrall N. Photonuclear reactions – From basic research to applications. *Prog. Part. Nucl. Phys.* 2022;122:article number 103903. doi: 10.1016/j.ppnp.2021.103903.

[2] Finch SW, Bhike M, Howell CR, Krishichayan, Tornow W, Tonchev AP. Measurements of short-lived isomers from photofission as a method of active interrogation for special nuclear materials. *Phys. Rev. Appl.* 2021;15:article number 034037. doi: 10.1103/PhysRevApplied.15.034037.

[3] Chin KW, Sagara H, Han CY. Application of photofission reaction to identify high-enriched uranium by bremsstrahlung photons. *Ann. Nucl. Energy*. 2021;158:article number 108295. doi: 10.1016/j.anucene.2021.108295.

[4] Delarue M, Simon E, Pérot B, Allinei P-G, Estre N, Eck D et al. New measurements of cumulative photofission yields of ^{239}Pu, ^{235}U and ^{238}Uwith a 17.5 MeV bremsstrahlung photon beam and progress toward actinide differentiation. *Nuclear Inst. and Methods in Physics Research, A*. 2022;1040:article number 167259. doi: 10.1016/j.nima.2022.167259.

[5] Dighe PM, Vinod M, Thombare SG, Prafulla S, Kamble NR, Kamble LP et al. Photofission method for quantification of fissile material in large drums. *Nucl. Instrum. Methods. Phys. Res., A*. 2019;946:article number 162624. doi: 10.1016/j.nima.2019.162624.

[6] Meleshenkovskii I, Elayeb A, De Stefano R, Sari A. Feasibility study of the photofission technique for radiological characterization of 220-L concrete-lined nuclear waste drums using 7 or 9 MeV linacs. *Nucl. Instrum. Methods Phys. Res., A.* 2022;1029:article number 166422. doi:10.1016/j.nima.2022.166422.

[7] Parlag OO, Masluyk VT, Dovbnja AM, Pylypchynets IV, Holovej VM, Lengyel AI. A method of stimulating delayed gamma radiation from fission products of actinide nuclei in hermetic stainless steel containers for identification of their isotopic composition. Patent of Ukraine for a utility model No. 133090. Bulletin No 6. March 25, 2019.

[8] Rudycheva VG, Azarenkova NA, Girkaa IA, Rudycheva YV. Bremsstrahlung generation by 7.5 MeV electrons in converters made of different materials. *East Eur. J. Phys.* 2021;3:91-6. doi: 10.26565/2312-4334-2021-3-14.

[9] Sahoo GS, Tripathy SP, Kulkarni MS. Simulation study on radiation fields around targets to apply CR-39 for photo-neutron measurement in electron accelerator near the threshold energy. *Applied Radiation and Isotopes*. 2022;181:article number 110080. doi: 10.1016/j.apradiso.2021.110080.

[10] Lisovska VV, Malykhina TV. Computer simulation of the angular distribution of electrons and bremsstrahlung photons in tantalum converter. *East Eur. J. Phys.* 2020;2:89-93. doi: 10.26565/2312-4334-2020-2-07.

[11] Anam C, Soejoko DS, Haryanto F, Yani S, Dougherty G. Electron contamination for 6 MV photon beams from an Elekta linac: Monte Carlo simulation. *Journal of Physics and Its Applications*. 2020;2(2):97-101. doi: 10.14710/jpa.v2i2.7771.

[12] Pomatsalyuk RI, Shevchenko VA, Titov DT, Tenishev AE, Uvarov VL, Zakharchenko AA, et al. Formation and monitoring of secondary X-ray radiation under product processing with electron beam. *Probl. At. Sci. Technol*. 2021;136(6):201-5. doi: 10.46813/2021-136-201.

[13] Didi A, Dadouch A, El Bekkouri H, Bencheikh M. Monte Carlo transport code use for optimisation of neutron flux produced with 10–18 MeV electron beam energy. *Int. J. Nucl. Energy Sci. Technol*. 2018;12(4):313-23. doi: 10.1504/IJNEST.2018.10018233.

[14] Banaee N, Goodarzi K, Nedaie HA. Neutron contamination in radiotherapy processes: a review study. *J. Radiat. Res.* 2021;62:947-54. doi: 10.1093/jrr/rrab076.

[15] Moghaddasi L, Colyer C. Evaluation of the effectiveness of steel for shielding photoneutrons produced in medical linear accelerators: A Monte Carlo particle transport study. *Phys. Med*. 2022;98:53-62. doi: 10.1016/j.ejmp.2022.04.009

[16] Parlag OO, Masluyk VT, Dovbnja AM, Holovej VM, Pylypchynets IV, Lengyel AI, et al. Application of boron carbide B4C for cleaning beams of bremsstrahlung radiation of electronic accelerators. Utility model patent No. 96384. Bulletin No. 3. February 10, 2015.

[17] Adeli R, Shirmardi SP, Ahmadi SJ. Theory and simulation investigation of low energy neutron shielding for different boron compounds. *J Test Eval*. 2016;45(5):article number 20160060. doi: 10.1520/JTE20160060.

[18] Afkham Y, Mesbahi A, Alemi A, Zolfagharpour F, Jabbari N. Design and fabrication of a nano-based neutron shield for fast neutrons from medical linear accelerators in radiation therapy. *Radiat. Oncol*. 2020;5:article number 105. doi: 10.1186/s13014-020-01551-1.

[19] Khabaz R. Effect of each component of a LINAC therapy head on neutron and photon spectra. *Appl. Radiat. Isot*. 2018;139:40-5. doi: 10.1016/j.apradiso.2018.04.022.

[20] Yania S., Budiansah I, Rhanic MF, Haryanto F. Monte Carlo model and output factors of Elekta infinity TM 6 and 10 MV photon beam. *Rep Pract Oncol Radiother*. 2020;25:470-478. doi: 10.1016/j.rpor.2020.03.021.

[21] Haysak II; Takhtasiev OV, Khushvaktov J, Solnyshkin AA, Tanchak A, Holomb RR, et al. Monte Carlo simulation of bremsstrahlung spectra for low energy electron accelerators. In: 2020 21st International Scientific Conference on Electric Power Engineering (EPE); 2020; Prague. Prague: IEEE; 2020. P. 1-4. doi:10.1109/EPE51172.2020.9269252.

[22] Meleshenkovskii I, Ogawa T, Sari A, Carrel F, Boudergui K. Optimization of a 9 MeV electron accelerator bremsstrahlung flux for photofission-based assay techniques using PHITS and MCNP6 Monte Carlo codes. *Nucl. Instrum. Methods Phys. Res. B*. 2020;(483):5-14. doi: 10.1016/j.nimb.2020.10.002.

[23] Silvaa VM, Cardoso DO, Vellozo SO. Experimental apparatus for measurement of photoneutrons from linear accelerator with energy of 16 MeV. *Braz. J. Rad. Sci.* 2021;(9):1-18. doi: 10.15392/bjrs.v9i3.1615.

[24] Meert CA, Panter AP, Jinia AJ, MacDonald AT, Clarke SD, Pierson BD, et al. High-fidelity photoneutron detection via neutron activation analysis. *Nucl. Instrum. Methods Phys. Res. A* 2022;(1040):article number 167116. doi: 10.1016/j.nima.2022.167116.

[25] GEANT 4. A simulation toolkit. Geant4 10.7 Software Download [Internet]. [updated 12/04/2020; cited 12/10/2022]. Available from: https://geant4.web.cern.ch/node/1914.

[26] Romanyuk MI, Hainysh JJ, Plakosh Y, Kovtun V, Turhovsky OM, Pitchenko GF, et al. Microtron M-30 for radiation experiments: Formation and control of irradiation fields. *Probl. At. Sci. Technol*. 2022;139(3):137-43. doi:10.46813/2022-139-137.

[27] Romanyuk MI, Gaynish JJ, Turhovsky OM, Goshovsky MV, Pitchenko GF, Megela IG, et al. Methods of formation and control of radiation fields of M-30 microtron. *J. Phys. Stud.* 2022;(26):article number 1201. doi: 10.30970/jps.26.1201.
[28] Pylypchynets IV, Parlag OO, Masluyk VT, Lengyel AI, Romanyuk MI, Megela IG, et al. Double-layer targets for forming the beams of the high-energy photons on the electron accelerator of M-30 microtron. *Scientific Herald of Uzhhorod University. Series "Physics".* 2019;(45):50-60. doi: 10.24144/2415-8038.2019.45.
[29] Haddad Kh, Anjak O, Yousef B. Neutron and high energy photon fluence estimation in CLINAC using gold activation foils. *Rep. Pract. Oncol. Radiother.* 2019;(24):41-6. doi: 10.1016/j.rpor.2018.08.009.
[30] Decay Radiation database version of 3/25/2022 [Internet]. [updated 3/25/2022; cited 12/15/2022]. Available from: https://www.nndc.bnl.gov/nudat3/indx_dec.jsp.
[31] Evaluated Nuclear Data File (ENDF). Database Version of 2022-04-22 [Internet]. [updated 04/22/2022; cited 11/30/2022]. Available from: https://www-nds.iaea.org/exfor/endf.htm.

Оптимальна схема стимуляції фотоподілу екранованих ядерних матеріалів на мікротроні М-30: комбінація теоретичних та експериментальних досліджень

Ігор Васильович Пилипчинець

аспірант, ORCID: https://orcid.org/0000-0002-0120-7703.
Інститут електронної фізики НАН України,
88017, вул. Університетська, 21, м. Ужгород, Україна

Анотація

Актуальність. Реакція фотоподілу екранованих ядерних матеріалів широко використовується для розробки методів неруйнівного аналізу їх ізотопного складу. Для стимуляції реакції фотоподілу використовуються пучки гальмівного випромінювання, отримані на електронних прискорювачах. Їх параметри суттєво залежать від конструктивних особливостей прискорювачів та схем активації зразків.

Мета. Теоретичне моделювання параметрів оптимальної схеми стимуляції реакції фотоподілу екранованих ядерних матеріалів на електронному прискорювачі – мікротроні М-30 для потреб аналізу їх ізотопного складу, з врахуванням його технічних характеристик, та експериментальна перевірка її параметрів.

Методологія. Теоретичні розрахунки параметрів пучків гальмівного випромінювання для мікротрону М-30 проводилися з застосуванням інструментарію "GEANT4". Для експериментальних досліджень впливу конструктивних елементів оптимальної схеми стимуляції на інтегральні характеристик гальмівних фотонів, вторинних фотонейтронів використано метод активації детекторів із золота; для залишкових електронів – метод пропускання на базі прохідної камери та циліндру Фарадея.

Результати. У результаті поєднання теоретичних і експериментальних досліджень встановлено оптимальні параметри схеми активації ядерних матеріалів на мікротроні М-30.Схема забезпечує експериментальні умови, за яких втрати пучків гальмівних фотонів, що взаємодіють із досліджуваними зразками (з енергіями $\geq$ 6 МеВ), не перевищують 35 % від їх початкових значень, при практичній відсутності залишкових електронів (98 % електронів поглинаються) і вторинних фотонейтронів (не більше 1E-9 n/e).

Висновки. Параметри, розробленої схеми стимуляції для мікротрону М-30, можуть бути застосовані для різних типів прискорювачів при врахуванні їх конструктивних особливостей, характеристик досліджуваних зразків і реалізованих схем активації

Ключові слова: гальмівне випромінювання, залишкові електрони, вторинні фотонейтрони, GEANT4, активаційний детектор, циліндр Фарадея

Scientific Herald of Uzhhorod University
Series "Physics"
Journal homepage: https://physics.uz.ua/en
Issue 52, 27-35
Received: 09/22/2022. Revised: 11/03/2022. Accepted: 11/22/2022

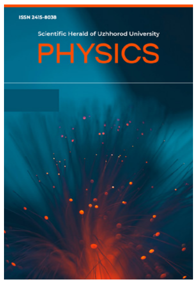

UDC 539.121.24
PACS 79.20.Hx, 34.80.Bm, 29.27.Bd, 02.70.Uu
DOI: 10.54919/2415-8038.2022.52.27-35

Electron modelling in conjunction witch vacuum modelling

Leonid Pavliuk*

ORCID: https://orcid.org/0000-0002-0260-2879.
Ohr Menachem Vinnitsa,
21000, 226 Mayakovskyi Str., Vinnytsia, Ukraine

Abstract

Relevance. The relevance of the study and the corresponding results is based on the need for digital transfer of scientific physical and mathematical devices for modelling the studied objects and phenomena of the real world into a digital programme environment, which forms a powerful research tool with the possibility of multi-reading and multi-vector calculation and forecasting of the nature and qualities of simulated elements of the physical world with a different scientifically based configuration of the initial data. The quality and reliability of digital models depend on the quality and completeness of consideration of various physical aspects in the simulated research objects and phenomena. Therefore, it is appropriate and relevant to formulate the initial iteration of digital transfer – the creation of a dependence-correlation apparatus. The second aspect that confirms the relevance of the current study is the fact that there is no integral model of the electron: currently, the world scientific community knows models describing individual characteristics and elements of the studied elementary particle, but there are no models describing the electron as an integral object.

Purpose. The purpose of the study is to develop a model of an electron associated with a simulated vacuum using appropriate analogue models from recognised fundamental studies.

Methodology. The study uses the methods of analogue Dirac models, spinor field models, the six-dimensional space-time model of the Bartini world, and the Planck oscillator model.

Results. Based on the results of experiments and physical and mathematical transformations in the current study, by integrating elements of the Ehrenfest paradox theory into the above models and basic elements of physical science, a complete model of the electron was formulated, which not only received a description of spatial and energy characteristics, but also allowed assessing the oetiological and morphological features of the development of the elementary particle, and individual physical and correlation dependencies were established.

Conclusions. First, the Hubble constant is necessary as a vacuum parameter in modelling elementary particles; second, the Hubble constant is included in the equation of the classical electron radius; and third, based on model calculations, the hypothesis of differences between the electron, muon, and tauon is proposed

Keywords: vacuum quantum, electron radius, magnetic moment, Hubble constant, Ehrenfest paradox

Suggested Citation:
Pavliuk L. Electron modelling in conjunction witch vacuum modelling. *Scientific Herald of Uzhhorod University. Series "Physics"*. 2022;(52):27-35.

*Corresponding author

Introduction

The relevance of the study follows from the trends in the development of the scientific sphere, which strives for deep diffusion involvement in the research environment of digital programme modelling tools, which provides not only a more structured and holistic physical picture of any phenomenon or process of manifestation of the real world, but also allows achieving the ability to predict the development of the studied objects with an acceptable degree of confidence. The basis of the qualitative transition of analogue processes to digital programme modelling (within the framework of global trends of the 4th iteration of the industrial progress of the multi-industry activity field) is a mathematical model adequate to real physical processes and conditions, the formula expressions and dependencies of which are the basis for the development of a software and digital model of objects and processes that carry out digital transfer. Software modelling of any physical phenomena and processes is as qualitative and adequate as the defined formula dependencies describing the studied aspects of real-world manifestations are more accurately and empirically converging. In the horizon of scientific research on the problems of simulation of electrons and electron-related processes, it is worth noting the studies by C. Lamy (on the possibility of using artificial neural networks for modelling non-local electron transport in plasma) [1], B. Tang (on numerical modelling of the processes of suprathermal electron transport in the solar wind) [2], X. An (on modelling the effects of bound electrons in the process of model studies of particles in a cell) [3], Y. Liu (on toroid modelling of electron loss processes flowing out of a 3D field in the organisation of research in the international experimental thermonuclear reactor (ITER)) [4], X. Li (on modelling the processes of acceleration and electron transfer in the early pulsed phase of a solar flare) [5], "Modelling of non-local electron transport in laser-driven double-ablation fronts" [6], "Relaxation of electron beams/strahls in solar outflows: observations vs. modelling" (on the correlated analysis of the results of modelling and full-scale measurements of electron beam/strahl relaxation processes in solar flows) [7], H. Funaba (on the study of the Thomson scattering effect in modelling and estimating electron temperature) [8], D. Vatansever et al. (on modelling surfaces that emit electrons when boundary layers are immersed in plasma) [9], V. Lazurik (on the investigation of semi-empirical models of electron beam control in radiation technologies) [10], O. Linder (on self-matching modelling of electron run-up during breakdowns in Tokamak (ITER)) [11], L. Adhikari (on modelling the process of heating protons and electrons in a fast solar wind) [12], M. Wibowo (on modelling the dynamics of ultra-fast electrons in strong magnetic fields using real-time electronic structure methods) [13], Y. Huang (on modelling strong electron heating by radio frequency waves at EAST) [14], Z. Wang (on real-time modelling and estimation of the total electron content in the vertical global ionosphere using hourly IGS data) [15]. When analysing these specialised publications, it was found that in modern physics, electron models only describe its properties. Known electron models do not answer questions about the structure of the electron, the nature of the electric charge, the nature of the fine structure constant, and the relationship between electron parameters and vacuum parameters. Building a model of an electron, in the study of which it is possible to establish new physical patterns, is an urgent task. As part of the current study, when modelling an electron in combination with vacuum modelling, oetiological and morphological features of the generation of the studied elementary particles are established, which provides a more complete physical picture of reality.

Materials and Methods

To achieve the established goals and objectives, the study uses recognised methods of microparticle modelling based on the application of analogue models implemented in accordance with the recommendations of R. Gaudenzi [16], A.J. Daley [17], V.V. Mdzinarishvili [18], S.D. Bass & E. Zohar [19], D. Hangleiter [20]. The use of these analogue models allowed involving in the process of target modelling the recognised physical-theoretical and physical-empirical formulations and dependencies, based on the results of integration of which the corresponding first-iterative calculations were performed. The electron model was developed in the following methodological sequence:

– the general parameters of the space-time continuum are determined, in particular, the concept of the density of matter determined using the gravitational constant and the Hubble constant;

– the model of physical vacuum is developed using the conceptual basis and theoretical background of P.A.M. Dirac models, spinor field models, di Bartini model of six-dimensional spacetime (Bartini world), and M.K.E.L. Planck oscillator model;

– the energy characteristics of the simulated vacuum are determined, in particular, the meager spinor energy, the electric field density, the energy due to the magnetic field, the oscillator energies, etc., the derived dependences of which allowed formulating the electron model (in particular, determining the spatial and energy parameters of the electron and the parameters of the membrane of the elementary particle under study);

– for the purpose of correlation and scientific evaluation of the developed model of the object under study, the previous scientific experience in modelling the electron as an elementary particle is established with the allocation of an appropriate vector for the development of analogue modelling with a focus on the model development directly for the studied atomic element associated with the vacuum model, in particular, by R. Solomon (on establishing the correlative dependence of the mass and Hubble constant of an electron on the environment) [21], G. Qu & G. Tatara (on the study of massive electrons by P.A.M. Dirac) [22], A. Uka & S. Nazarko (on the use of di Bartini models in energy expression and the use of spatial parameters to achieve unification based on the ideas of Einstein and Wheeler) [23], H.P. Le (on quantum modeling of Fokker – M.K.E.L. Planck degenerate electrons) [24], L. Nash (on the dynamics of Euclidean space-time at the M.K.E.L. Planck scale) [25], J. Walkowiak (on approximate atomic models for fast calculation of the Fokker – M.K.E.L. Planck equation in thermonuclear plasma with high Z impurities and superthermal electrons) [26];

– the parameters of the electron for which it is advisable to perform modelling are determined;

– analogue models are used to develop an electron model with the appropriate definition of derived quantities that establish the simulation quality and physical parameters of the model;

– the energy parameters of the generated electron model are calculated;

– a correlation is established between the parameters of the simulated electron and Hubble's fundamental studies, in particular, on the direct participation of the Hubble constant in the development of the electron model.

Based on the results of modelling with the development of an appropriate mathematical framework (based on specialised physical and empirical formulations and expressions), analytical conclusions are formed regarding the scientific value of the developed model of an electron associated with vacuum modelling and the presence of a correlative relationship with recognised aspects of the physical picture of the real world.

Results and Discussion

The space-time continuum is characterised by a critical density of matter [21]:

$$\rho = \frac{3H^2}{8\pi G}, \quad (1)$$

where G – gravitational constant; H – Hubble constant. ($H = 3 \cdot 10^{-18} c^{-1} \div 4 \cdot 10^{-18} c^{-1}$).

Known models of physical vacuum:

– model proposed by P.A.M. Dirac, where vacuum is considered as an environment consisting of pairs of particles and antiparticles;

– models of spinor fields, where the vacuum is considered an environment consisting of non-mass spinors [22].

There is also a well-known theory of the (3+3)-dimensional continuum (Bartini world), which was developed by a prominent aircraft designer, theoretical physicist, cosmologist, and philosopher R.O. di Bartini [23]. He considered his six-dimensional space-time to be quantum. As the quantum of space, R.O. di Bartini [23] adopted the classical electron radius. Assuming that the vacuum is quantum, there is an element of the microstructure of the vacuum – a particle with a spin $\frac{\hbar}{2}$, with localisation radius r_0 and a density ρ equal in magnitude to the critical density of the space-time continuum. The meager spinor energy is equal to the product of the density by the volume of the localisation sphere and the square of the speed of light:

$$W = \frac{H^2 r_0^3 c^2}{2G} \quad (2)$$

This minuscule energy is equated with the minuscule energy of a vacuum quantum $\frac{\hbar}{2}H$ and after algebraic transformations, the radius of the spherical surface equal to the classical radius of the electron is obtained:

$$r_0 = \left(\frac{G\hbar}{Hc^2}\right)^{\frac{1}{3}} \quad (3)$$

Classical electron radius r_0 – a fundamental constant of the length dimension, which is included in a number of equations of classical and quantum electrodynamics. From equation (3), it is advisable to express and perform a numerical calculation of the Hubble constant, since only its approximate value is known in physics. Calculated value: $H \approx 3{,}5 \cdot 10^{-18} c^{-1}$.

The modelling technique requires the established formulas to be derived from other model constructions. For the first time, the membrane model of the Electron was proposed by P.A.M. Dirac [22]. The elementary charge in his model is evenly distributed over the spherical surface of the membrane. Next, the study considers the membrane model of an electron, with the following model constructions. One spatial coordinate from a three-dimensional space is collapsed, compacted, and its thickness is minimised. The resulting membrane has the following surface density:

$$\sigma = \frac{cH}{8\pi G} \quad (4)$$

Equation (4) was obtained by multiplying the critical density value ρ by the volume of a sphere with a radius c/H and dividing the resulting mass by the surface area of this sphere. The surface energy density of the membrane correlates with the energy density of the electric field of an electron:

$$w = g\sigma, \quad (5)$$

where g – parameter with the acceleration dimension.

Electric field energy density:

$$w = \frac{\varepsilon_0 E^2}{2}, \quad (6)$$

where E – electric field strength; ε_0 – electric constant.

Thus, the parameters of the two-dimensional electric field of an electron are correlated with the parameters of a two-dimensional membrane. The magnetic field of an electron is characterised by one-dimensionality – the magnetic moment of the electron (N.H.D. Bohr magneton) is projected in any fixed direction, taking the value $\pm\mu_Б$. Thus, a one-dimensional continuum element is observed in three-dimensional space. The study provides a mechanical analogy of the N.H.D. Bohr magneton. Let the tube be fixed at one end in the swivel joint. A miniature robot inside the tube captures freedom of movement in one coordinate. For him, space is one-dimensional. The observer in a three-dimensional space records different positions of the tube, which has two degrees of freedom of rotational motion, and notes its constant length. The realisation of an electron in a space-time continuum is associated with the splitting of three-dimensional space into two-dimensional and one-dimensional. In this case, the charge sign is determined by the symmetry variants of the space-time continuum. Mass of a spherical membrane with radius r_0 is equal to $4\pi\sigma r_0^2$, and the energy corresponding to this mass is equal to:

$$W_e = \frac{H r_0^2 c^3}{2G} \tag{7}$$

This energy can be identified as conditioned by an electric field. The value c/r_0, which has the dimension of the cyclic frequency, is denoted by the letter ω_0. Then, by analogy with rotational motion, the energy conditioned by the magnetic field:

$$W_m = \frac{\hbar}{2}\cdot\omega_0 = \frac{\hbar c}{2r_0} \tag{8}$$

By analogy with an electromagnetic oscillator or with an electromagnetic standing wave, where the energy of the electric and magnetic fields are equal, the right-hand sides of equations (7, 8) are equated, and the equation (3) of the classical electron radius is obtained from the resulting equality. The bar frequency is determined by the equation:

$$\omega_p = \left(\frac{c^5}{G\hbar}\right)^{\frac{1}{2}} \tag{9}$$

Then, a compact formula for the electron is obtained from equation (3):

$$\omega_0 = \left(H\omega_p^2\right)^{\frac{1}{3}} \tag{10}$$

Next, as an analogue, the study considers a model of the rotational motion of a ring or cylindrical surface rotating around its axis at a linear speed close to the speed of light. In this case, there is a paradox of the special theory of relativity, formulated by P. Ehrenfest in 1909. The essence of the paradox is that the velocity of each element of the ring is directed tangentially and the ring must undergo Lorentz reduction in length. Then, for an external observer, the ratio of the ring length to its radius will not be equal to 2π and, accordingly, the positions of the Euclid geometry are not met. However, when formulating the paradox, the phenomenon of relativistic aberration of light was not taken into account. From the special theory of relativity, it is known that the direction of light propagation transverse to the velocity V will be for an external observer at an angle θ to the velocity V [27]. Then:

$$cos\ cos\ \theta = \frac{V}{c} \tag{11}$$

The wavelength of light in this direction is reduced due to the C. Doppler effect. In the rotating ring model, this is manifested by a reduction in the length of the radius. Thus, in the relativistic case, the radius of rotational motion, i.e., the radius along which the centripetal force acts, is directed at an angle θ to the linear velocity of the ring elements and equal to:

$$R = R_0\left(1 - \frac{V^2}{c^2}\right)^{\frac{1}{2}}, \tag{12}$$

where R_0 – geometric radius of the ring.

The centre of a circle is not a point, but an inner sphere with a radius $\frac{R_0 V}{c}$, to which radius R is directed tangentially (Figure 1).

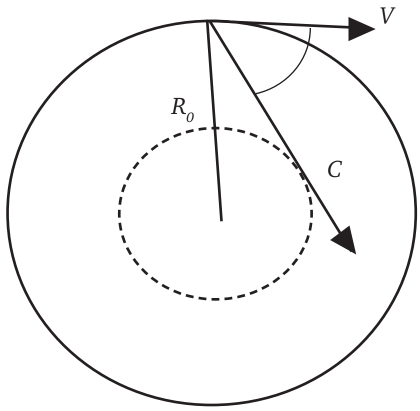

Figure 1. Concept diagram of a model environment for determining electron parameters

Shortening the length of the radius of rotational motion along which the centripetal force acts can be defined as compressing or folding a single spatial coordinate. When the ring moves with linear acceleration, there are two possible options:

1. Acceleration with a "+" sign and the spatial coordinate collapses.
2. Acceleration with a "-" sign and the spatial coordinate unfolds.

Obviously, by analogy with the model of a rotating ring, in an electron and positron, there is a convolution or sweep of one spatial coordinate and the implementation of a two-dimensional membrane. The acceleration sign determines the charge sign of the particle.

Next, the study environment considers the oscillator model by M.K.E.L. Planck [28; 29]. According to Planck's quantum hypothesis, the energy of an oscillator can only take certain discrete values equal to an integer number of elementary portions of energy – energy quanta. According to the theory of M.K.E.L. Planck, the average value of the oscillator energy with frequency ν is determined by the equation [28; 29]:

$$\langle E_\nu \rangle = \frac{h\nu}{expexp\left(\frac{h\nu}{kT}\right) - 1}, \tag{13}$$

where k – Boltzmann constant; T – radiation temperature of the oscillator.

In accordance with law of W. Wien, the frequency ν is related to the radiation temperature by the ratio [30]:

$$T = \frac{b\nu}{c}, \tag{14}$$

where Wien's constant b is determined by the equation:

$$b = \frac{hc}{4{,}965k} \tag{15}$$

Thus, b=2.9·10^{-3} mK. Substituting equations (14) and (15) into equation (13), the following is obtained after algebraic transformations:

$$\langle E_\nu \rangle = \frac{h\nu}{expexp\,(4{,}965) - 1} \approx \frac{h\nu}{143} \tag{16}$$

The coefficient 1/143 was obtained for the M.K.E.L. Planck oscillator model [28; 29]. Interestingly, there is a similar coefficient for an electron. This is the so-called fine structure constant:

$$\alpha \approx \frac{1}{137} \tag{17}$$

That is, for an electron, the following equation is valid:

$$m_0 c^2 = \alpha \hbar \omega_0 \tag{18}$$

where m_0 – the rest mass of the electron.

The physical nature of the fine structure constant in modern physics is unknown. There is also no comprehensive knowledge of the structure of the electron. Therefore, it is premature to comment on the obtained ratios of physical quantities. Next, the study calculates physical quantities that have the dimension of limit frequencies. A well-known equation that is required for calculations [31; 32]:

$$e^2 = \alpha 4\pi\varepsilon_0 \hbar c \tag{19}$$

where e – elementary charge.

As a result of algebraic transformations, the following is obtained from equation (5):

$$\frac{\varepsilon_0 E^2}{2} = g\sigma$$
$$\frac{e^2}{4\pi\varepsilon_0 r^4} = \frac{gcH}{G}$$
$$\frac{\alpha\hbar c}{r^4} = \frac{gcH}{G} \tag{20}$$
$$\left(\frac{c}{r}\right)^4 = \frac{g\alpha^{-1}}{c} \cdot H\omega_p^2$$

Equation $f = \frac{g\alpha^{-1}}{c}$ has a frequency dimension. Values of f within the lowest and highest possible frequencies in nature:

$$H < f < \omega_p \tag{21}$$

Then the possible frequencies in the mathematical model of the oscillator are within:

$$\left(H\omega_p\right)^{\frac{1}{2}} < \frac{c}{r} < \left(H\omega_p^3\right)^{\frac{1}{4}} \tag{22}$$

The frequency of the upper limit corresponds to the frequency of the fermium energy quantum. It is known that in particle accelerators, an electron can be given an energy not exceeding 294 GeV [33]. This is the value of the fermium energy of the weak interaction. Numerical calculations in the first approximation confirm the ratio. Next, the study considers the nature of the lower frequency limit.

Analysing the spectra of galaxies, E.P. Hubble [34] concluded that most galaxies are moving away from us at speeds proportional to their distance. Galaxies are moving away not only from our galaxy, but also from each other. The universe bound by the law of E.P. Hubble, the same for an observer located at any point in space. The fundamental fact of observation is that the absorption lines in the spectra of nearby galaxies are shifted towards the red part of the spectrum [34].

Two types of redshift are known: Doppler and gravitational. In the 1920s, the general theory of relativity was not yet as widespread as it is now. Therefore, it is natural that observers interpreted the red shift in the spectra of galaxies as Doppler. But in modern cosmological theories, the expansion of the universe is related to the curvature of the space-time continuum, which is equivalent to a gravitational field. The Doppler and gravitational redshifts are equivalent when deriving the E.P. Hubble law [34] and are described by the equation:

$$\nu = \left(1 - \frac{Hl}{c}\right)\nu_0 \quad (23)$$

where ν_0 – frequency of light emitted by the object; ν – frequency of light reaching the observer; l – distance from the object to the observer.

The equivalence of Doppler and gravitational redshifts allows introducing into theoretical calculations a value with the dimension of the potential of the gravitational field [35]:

$$(1 + \varphi) = \left(1 - \frac{Hl}{c}\right) \quad (24)$$

The distance $r=l$ from a compact object with mass M is determined, on which the potential of its gravitational field is equal to:

$$(1 + \varphi) = \left(1 - \frac{GM}{c^2 r}\right) \quad (25)$$

From equations (24, 25), the following is obtained:

$$r = \left(\frac{GM}{cH}\right)^{\frac{1}{2}} \quad (26)$$

Next, the study determines at what value of r the mass of a microparticle has the value:

$$r = \left(\frac{G\hbar}{Hc^2}\right)^{\frac{1}{3}} \quad (27)$$

Equation (27) is substituted into equation (26) and after algebraic transformations:

$$r = \left(\frac{G\hbar}{Hc^2}\right)^{\frac{1}{3}} \quad (28)$$

The formula for the classical electron radius in the third model construction is obtained. The Planck mass is expressed by the equation:

$$m_p = \left(\frac{\hbar c}{G}\right)^{\frac{1}{2}} = \frac{\hbar\omega_p}{c^2} \quad (29)$$

The distance r_1 is defined for Plank mass:

$$r_1 = \left(\frac{Gm_p}{cH}\right)^{\frac{1}{2}} = \frac{c}{(H\omega_p)^{\frac{1}{2}}} \quad (30)$$

The denominator in equation (30) is the value of the lower limit of the frequency f in equation (22). Interestingly, the surface density of a membrane with a Planck mass and a spherical surface radius r_1 amounts to 2σ.

Elementary particles (electrons, muons, and tauons) belong to the class of leptons. It is a well-known hypothesis that muons and tauons are states of an excited electron. The main provisions of the theory of the six-dimensional world developed by R.O. di Bartini are used as a basis for model constructions [23]. In this model, in addition to the usual Cartesian coordinates of three-dimensional space, R.O. di Bartini [23] proposed to consider the same three-dimensional time model with three orthogonal coordinate axes. Physical phenomena of the microcosm, in particular, the crushing of elementary particles into quarks, suggest the application of the theory of R.O. di Bartini [23] in particle physics. In the (3+3)-dimensional continuum of the microcosm, it is possible to implement the addition of mutually perpendicular velocity fluctuations. Analogue models with calculations based on the formulas of relativistic addition of velocities are published in [36].

Let in the relativistic case be mutually perpendicular fluctuations in the velocity of a material point at the same oscillation frequency and phase difference. Setting the values of the speeds at which circular motion can be implemented:

$$V_x = c\, sin\, sin\, \omega t \quad (31)$$

$$V_y = c\, cos\, cos\, \omega t \quad (32)$$

$$V_z = c\, cos\, cos\, \omega t \quad (33)$$

where c – speed of light in a vacuum.

In accordance with the law of relativistic addition of velocities, the resulting velocity when adding mutually perpendicular vibrations is equal to:

$$V_\mu = \left(V_x^2 + V_y^2 - \frac{V_x^2 V_y^2}{c^2}\right)^{\frac{1}{2}} \quad (34)$$

Substituting equations (31) and (32) into equation (34), and after algebraic transformations, the following is obtained:

$$V_\mu = c(1 - 0.25 \cdot sin^2 2\omega t)^{\frac{1}{2}} \quad (35)$$

Therefore, the resulting linear velocity of circular motion is pulsating.

In the case of relativistic addition of mutually perpendicular velocity fluctuations along three Cartesian coordinate axes, the resulting velocity is equal to:

$$V_\tau = \left(V_x^2 + V_y^2 + V_z^2 - \frac{V_x^2 V_y^2}{c^2} - \frac{V_x^2 V_z^2}{c^2} - \frac{V_y^2 V_z^2}{c^2} + \frac{V_x^2 V_y^2 V_z^2}{c^4}\right)^{\frac{1}{2}} \quad (36)$$

Substituting the values of velocities from equations (31-33) into equation (36) and after algebraic calculations, the following is obtained:

$$V_\tau = c(1 - 0.25 sin^2 2\omega t \cdot cos^2 \omega t)^{\frac{1}{2}} \quad (37)$$

Pulsations of the resulting velocities in analogue models give an idea of the nature of the excited states of the electron, which are manifested in the implementation of the muon and tauon.

Conclusions

In the current study, in accordance with the formulated goal and the identified scientific problem regarding the absence of electron models in the scientific space (moreover, in combination with the vacuum model), proper results were obtained.

With the help of a multilocal literature review, it is established that currently existing mathematical and physical models carry out model reproduction of only certain characteristics of the studied elementary particle, while the entire object of research (electron) (according to scientific research in the current chronometric horizon) is not reproduced in any of the relevant specialised studies in the digital model environment.

It is established that modelling with the development of an appropriate mathematical framework (through algebraic transformations) for a certain scientific aspect under study (development of an integral electron model) can be carried out using analogue models and corresponding recognised scientific results of modelling spinor fields, modelling six-dimensional space-time, and modelling an oscillator.

Using recognised scientific results, a model of the electron is created that reproduces not only its spatial and energy characteristics, but also determines the oetiological and morphological features of the generation of the elementary particle under study, which provides a more complete physical picture of reality.

When modelling the electron in combination with vacuum modelling, it became obvious that the constant is a vacuum parameter necessary for modelling and calculating elementary particles. The simulation results allow going beyond the paradigms of modern physics. It becomes obvious that elementary particles are not just material objects in the void of vacuum, but are created as a result of its splitting, crushing, oscillating movements, and interaction with vacuum quanta.

The prospect of further development of models consists in visual modelling of elementary particles made up of quarks as oscillating systems in which the distance between the components is a multiple of $\lambda/4$ and the transfer of the obtained physical and mathematical framework to a digital program environment for the development of an already direct electronic model of the elementary particle under study.

References

[1] Lamy C, Dubroca B, Nicola P, Tikhonchuk V, Feugeas J-L. Modeling of electron nonlocal transport in plasmas using artificial neural networks. *Phys. Rev. E*, 2022;(105):article number 055201.

[2] Tang B, Zank GP, Kolobov VI. Numerical modeling of suprathermal electron transport in the solar wind: Effects of whistler turbulence with a full diffusion tensor. *The Astrophys. J*, 2022;(924(2)):1-13.

[3] An X, Chen M, Sheng Z-M, Zhang J. Modeling of bound electron effects in particle-in-cell simulation. *Communic. in Computat. Phys*. 2022;(32):583-94.

[4] Liu Y, Aleynikova K, Paz-Soldan C, Aleynikov P, Lukash V, Khayrutdinov R. Toroidal modeling of runaway electron loss due to 3D fields in ITER. *Nucl. Fus*. 2022;(62(6)):article number 066026.

[5] Li X, Guo F, Chen B, Shen C, Glesener L. Modeling electron acceleration and transport in the early impulsive phase of the 2017 September 10 solar flare. *The Astrophys. J.* 2022;(932(2)):article number 04946.

[6] Modeling of nonlocal electron transport in laser-driven double-ablation fronts. [Internet]. 2022. Available from: http/meetings.aps.org/Meeting/DPP22/Session/PO04.9.

[7] Relaxation of electron beams/strahls in solar outflows: observations vs. modeling. [Internet]. 2022. Available from: http/ui.adsabs.harvard.edu/abs/2022cosp...44.1668L/abstract.

[8] Funaba H, Yamada I, Yasuhara R, Uehara H, Tojo H, Yatsuka E, et al. Fast signal modeling for Thomson scattering diagnostics and effects on electron temperature evaluation. *Plas. and Fus. Resear.* 2022;(17):number article 2402032.

[9] Vatansever D, Nuwal N, Levin DA. Modeling of electron emitting surfaces submersed in boundary layer plasmas. In: 2022 IEEE International Conference on Plasma Science (ICOPS). New York: IEEE Publishing; 2022. P. 1-2.

[10] Lazurik V, Sawan S, Lazurik V, Rudychev V. Semi-empirical models of electron beam control in radiation technologies. In: 2022 IEEE 2nd International Maghreb Meeting of the Conference on Sciences and Techniques of Automatic Control and Computer Engineering (MI-STA). New York: IEEE Publishing; 2022. P. 27-31.

[11] Linder O. Self-consistent modeling of electron runaway in tokamak disruptions. Munich: Technische Universität München; 2022.

[12] Adhikari L, Zank GP, Zhao L-L, Nakanotani M, Tasnim S. Modeling proton and electron heating in the fast solar wind. *Astron. & Astrophys*. 2021;(650):23-30.

[13] Wibowo M, Irons TJ, Teale AM. Modeling ultrafast electron dynamics in strong magnetic fields using real-time time-dependent electronic structure methods. *J. of Chem. Theory and Computat.* 2021;(17(4)):2137-165.

[14] Huang Y, Xiang N, Chen J, Ma L, Li E, Gong X, et al. Modeling very high electron heating by radio frequency waves on EAST. *Nuclear Fusion*. 2021;(61(9)):article number 096026.

[15] Wang Z, Xue K, Wang C, Zhang T, Fan L, Hu Z, et al. Near real-time modeling of global ionospheric vertical total electron content using hourly IGS data. *Chinese J. of Aeronaut.* 2021;(34(2)):386-95.

[16] Gaudenzi R. Elementary particles as excitations of a solid medium. Is the universe a superconductor? In: Historical roots of spontaneous symmetry breaking. Berlin: Springer; 2022. P. 69-112.

[17] Daley AJ, Bloch I, Kokail C, Flannigan S, Pearson N, Troyer M, et al. Practical quantum advantage in quantum simulation. *Nature*. 2022;(607):667-76.
[18] Mdzinarishvili VV. New models of the physical microcosm and their optimality. *Open Access Libr. J*. 2022;(9(5)):1-20.
[19] Bass SD, Zohar E. Quantum technologies in particle physics. *Philos. Transact. of the Royal Society A*. 2022;(380):article number 20210072.
[20] Hangleiter D, Carolan J, Thébault KP. Analogue quantum simulation: A new instrument for scientific understanding. Berlin: Springer Nature; 2022.
[21] Solomon R, Agarwal G, Stojkovic D. Environment dependent electron mass and the Hubble constant tension. *Phys. Review D*. 2022;(105(10)):article number 103536.
[22] Qu G, Tatara G. The inverse faraday effect in the massive dirac electrons. *Phys. Review B*. 2022;(106):article number 094414.
[23] Uka A, Nazarko S. New expression of energy and the use of spatial parameters to achieve unification based on the ideas of Einstein and Wheeler. In: The Fifteenth Marcel Grossmann Meeting: On recent developments in theoretical and experimental general relativity, astrophysics, and relativistic field theories. Singapore: World Scientific Publishing; 2022. P. 792-02.
[24] Le HP. Quantum Fokker-Planck modeling of degenerate electrons. *J. of Computat. Physics*. 2021;(434):article number 110230.
[25] Nash L. On the dynamics of Euclidean space-time at the Planck scale. *Reports in Advances of Phys. Sciences*. 2022;(3):article number 2250002.
[26] Walkowiak J, Jardin A, Bielecki J, Peysson Y, Mazon D, Dworak D, et al. Approximate atomic models for fast computation of the Fokker-Planck equation in fusion plasmas with high-Z impurities and suprathermal electrons. *Physics of Plasmas*. 2022;(29):article number 022501.
[27] Konstantinou G, Kyriakou K, Moulopoulos K. 2016. Emergent non-Hermitian contributions to the Ehrenfest and Hellmann-Feynman theorems. *Academia.* 2016;(1):7-15.
[28] Daywitt WC. The cosmic microwave background radiation as viewed in the Planck vacuum theory. *Europ. J. of Applied Physics*. 2022;(4(1)):27-8.
[29] Li T, Yan Y, Shi Q. A low-temperature quantum Fokker-Planck equation that improves the numerical stability of the hierarchical equations of motion for the Brownian oscillator spectral density. *The J. of Chem. Phys*. 2022;(156(6)):article number 064107.
[30] Ghosal P, Ray R. Probability distribution for black hole evaporation. *Physical Review D.* 2022;(105):article number 124016.
[31] Martins CJAP, Ferreira FPSA, Marto PV. Varying fine-structure constant cosmography. *Physics Letters B*. 2022;(827):article number 137002.
[32] Cui Q. Revisiting gravity, fine-structure constant, speed of light, and mass-energy equation through cosmic microwave background. *J. of Modern Physics*. 2022;(13(7)):1045-52.
[33] Chang, M., Ge, Y., Sheng, L. Generalization of the theory of three-dimensional quantum Hall effect of Fermi arcs in Weyl semimetal. *Chinese Physics B.* 2022;(31(5)):article number 057304.
[34] Pérez-García MA, Izzo L, Barba-González D, Bulla M, Sagués-Carracedo A, Pérez E, et al. 2022. Hubble constant and nuclear equation of state from kilonova spectro-photometric light curves. *Astr. & Astrophys*. 2022;(666):article number 134049.
[35] Pavliuk LO. Hubble's constant in the physics of the gravitational field. In: Modern research in world science. Proceedings of the 6rd International Scientific and Practical Conference. Lviv: SPC. 2022; P. 289-94.
[36] Pavliuk LO. Relativistic addition of mutually perpendicular oscillations as an analogue in modeling the muon and taon. *Sci-Article*. 2021;(95):article number 162066.

Моделювання електрона в поєднанні з моделюванням вакууму

Леонід Олексійович Павлюк

ORCID: https://orcid.org/0000-0002-0260-2879.
Приватний заклад «Ор Менахем Вінниця»
21000, вул. Маяковського, 226, м. Вінниця, Україна

Анотація

Актуальність. Актуальність дослідження та відповідних результатів формується з урахуванням необхідності здійснення цифрового трасферинга наукових фізико-математичних апаратів моделювання досліджуваних об'єктів та явищ реального світу в цифропрограмне середовище, що формує потужній дослідницький інструмент можливістю багатоітераційного та різновекторного обчислення та прогнозування характеру та якостей змодельованих елементів фізичної картини світу з різною науково обґрунтованою конфігурацією вихідних даних. Якість та достовірність цифрових моделей залежить від якості та повноти врахування різних фізичних аспектів в модельованих дослідницьких об'єктах та явищах. Відтак, доцільним та актуальним є формулювання початкової ітерації цифрового трансферингу – створення залежністно-кореляційного апарату. Другим аспектом, що засвідчує актуальність поточного дослідження є факт відсутності цілісної моделі електрону: наразі у світовій науковій спільноті відомі моделі, що описують окремі характеристики та елементи досліджуваної елементарної частинки, проте моделі, що описувала б електрон як цілісний об'єкт – відсутні.

Мета. Мета статті – розробка моделі електрону, що пов'язана з модельованим вакуумом з використанням відповідних аналогових моделей визнаних фундаментальних наукових праць.

Методологія. В поточному дослідженні використані методи аналогових діракових моделей, моделей спінорних полів, модель шестивимірного простору-часу бартінівського світу та модель планківського осцилятору.

Результати. За результатами дослідів та фізико-математичних трансформацій у поточному дослідженні шляхом інтеграції елементів теорії еренфестського парадоксу в зазначені вище моделі та базові елементи фізичної науки сформулювана цілісна модель електрону, яка не лише отримала опис просторових та енергетичних характеристик, а й дозволила оцінити етіолого-морфологічні особливості формування досліджуваної елементарної частинки, а також встановлені окремі фізико-кореляційні залежності.

Висновки. По-перше, хабблова постійна необхідна як параметр вакууму при моделюванні елементарних частинок, по-друге, хаблова постійна входить до формули класичного радіуса електрона, по-третє, на основі розрахунків моделей запропонована гіпотеза відмінностей електрона, мюона і таона

Ключові слова: квант вакууму, радіус електрона, магнітний момент, постійна Хаббла, парадокс Еренфеста

Scientific Herald of Uzhhorod University
Series "Physics"

Journal homepage: https://physics.uz.ua/en
Issue 52, 36-45
Received: 10/11/2022. Revised: 11/23/2022. Accepted: 12/15/2022

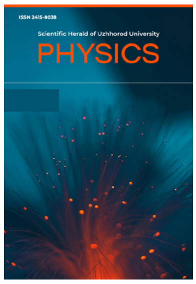

UDC 53.06
PACS 25.40.Sc 28.65.+a 24.10.Lx
DOI: 10.54919/2415-8038.2022.52.36-45

Research of spallation reaction on plutonium target irradiated by protons with energy of 660 MeV

Anhelina Tanchak[1*], Karel Katovsky[2], Ivan Haysak[3], Jindrich Adam[4], Robert Holomb[5]

[1]Postgraduate Student, ORCID: https://orcid.org/0000-0001-6566-7007.
Brno University of Technology, 60190, 548/1 Antonínská, Brno, Czech Republic

[2]PhD in Technical Sciences, Associate Professor, ORCID: https://orcid.org/0000-0001-9335-8199.
Brno University of Technology, 60190, 548/1 Antonínská, Brno, Czech Republic

[3]PhD in Physics and Mathematics, ORCID: https://orcid.org/0000-0003-4643-187X.
Uzhhorod National University, 88000, 3 Narodna Sq., Uzhhorod, Ukraine

[4]PhD in Technical Sciences, ORCID: https://orcid.org/0000-0002-9850-7007.
Brno University of Technology, 60190, 548/1 Antonínská, Brno, Czech Republic

[5]Postgraduate Student, ORCID: https://orcid.org/0000-0001-7918-7581.
Brno University of Technology, 60190, 548/1 Antonínská, Brno, Czech Republic

Abstract

Relevance. This paper describes the measurement of the cross sections of the fission and fragmentation reactions of a plutonium target irradiated with a series of protons characterized by an energy of 660 MeV at the Phazotron accelerator of the Joint Institute for Nuclear Research.

Purpose. The experiment focuses on the determination of short-lived radionuclides.

Methods. The experimental sample was measured in offline mode using gamma spectrometry with HPGe detector. The reaction rates of the formed residual nuclei were studied. The products of spallation reaction were determined with the help of the direct kinematics method. The DEIMOS32 software was used to process γ-spectra.

Results. As a result of the interaction of nuclear elements with protons, nuclei were formed in the ^{239}Pu sample. Those nuclei were identified using the TJ02000321–V3 software. The reaction products were identified based on gamma energies, intensity and half-life after the measurement set. During the study of the gamma spectra determined for the irradiated plutonium target, it was possible to establish 50 gamma lines and reveal 31 nuclides by energy and half-life cycles from 14.4 m to 3.19 h. The measured nuclear reaction cross-sections can serve as reference data for theoretical simulations of the interaction of protons with ^{239}Pu and they can be a supplement to the nuclear databases.

Conclusions. The obtained experimental result is compared with the simulation on MCNP 6.1. The data overall correspond to the expected range, but it still needs more evaluation. The next logical step is to search for primary products (mother nuclei) and compare the obtained experimental data with the results of computer simulations

Keywords: Phasotron accelerator, TJ02000321–V3 software, gamma spectra, radionuclides, γ-spectroscopy, accelerator-driven systems

Suggested Citation:
Tanchak A., Katovsky K, Haysak II, Adam JJ, Holomb RR. Research of spallation reaction on plutonium target irradiated by protons with energy of 660 MeV. *Scientific Herald of Uzhhorod University. Series "Physics".* 2022;(52):36-45.

*Corresponding author

Introduction

Given the large number of nuclear power plants around the world and plans to build new ones, it is safe to say that nuclear power continues to play an important role in the industry. At the same time, one of the biggest problems facing nuclear energy is still highly radioactive material produced during energy production.

An extremely important place in the policy of the world's leading states is occupied by the environmental vector, namely processing and working with waste generated during the operation of nuclear power plants. The issue of processing or domestic sale of weapons of plutonium and highly enriched uranium is urgent among the international community. This is especially true of countries that possess nuclear weapons, which brings about constant updating of approaches to the regulation of this sphere. Such programs will be developed in Europe, North America, Japan and russia [1-3]. According to the IAEA, in 2018 the volume of all exploited nuclear fuel in the world has reached 330.000 tons [4].

The composition of exploited energy resources includes uranium (≈96%), plutonium (≈1%) and high-level radioactive waste (≈3%). Uranium with a fission of less than 1% ^{235}U and plutonium can be reused. The products formed as a result of the exploitation of energy resources and their processing should be classified depending on their chemical composition into uranium, plutonium, and high-level waste.

Plutonium is the only transuranic element that is released and used on a large scale. Plutonium is better as a fuel for energy production because the fission reaction of one nucleus usually forms 3 new neutrons. Plutonium can be used in nuclear reactors from two sources: as a fission product in reactors of ^{238}U isotope; or excess plutonium created for atomic bombs [5]. By solving the problems and issues that arise in nuclear policy, with the help of nuclear fission energy, it is possible to provide permanent electric resources with a base load.

Accelerator-driven nuclear cross-section (ADS) data obtained by the subcritical system will help future researchers in the field of nuclear technology [6].

As for solving the issue of transmutation of highly active nuclear products, it is advisable to implement this process based on the approach using accelerators (ADS). These systems have a higher margin of safety due to their ability to stop the chain reaction by stopping the supply of protons.

Materials and Methods

In this experiment, direct kinematics method [7; 8] was used for determining spallation products. In this method, relativistic light projectile hits a heavy target. Using γ-spectroscopy and mass spectrometry, the cleavage products are detected and stopped at the target. Gamma-ray spectrometry is used to identify radionuclides and to measure their activity. Gamma-ray spectra were obtained from experimental results and prepared using the DEIMOS program. The spectrum is the main part of determining the experimental rates of the reaction products.

As a result of the implementation of the intranuclear cycle, as well as differentiation, fragmentation, evaporation of light nuclei and nucleons, the nuclei of the operated object are formed in connection with protons located in the target nucleus. The general form for this process is:

$$ {}^{A_T}_{Z_T}T(p,x){}^{A}_{Z}N \tag{1} $$

where, (p, x) expresses the type of nuclear reaction, *T* and *N* are the chemical objects of the target nucleus and the element, *AT* and *ZT* are the mass number and charge of the target nuclide, *A* and *Z* are the mass number and charge of the nuclide resulting from the nuclear reaction. The yields of radioactive products nuclear reaction are determining:

$$ R = \sigma(E) \cdot \Phi(E) \tag{2} $$

where σ(*E*) – cross sections of a nuclide production and Φ(*E*) is the proton flux density.

The number of formed residual nuclei Q (Ar, Zr) per atom in the sample N_A and one incident deuteron per second N_D form the reaction rate, which is determined by the equation (Fig. 1).

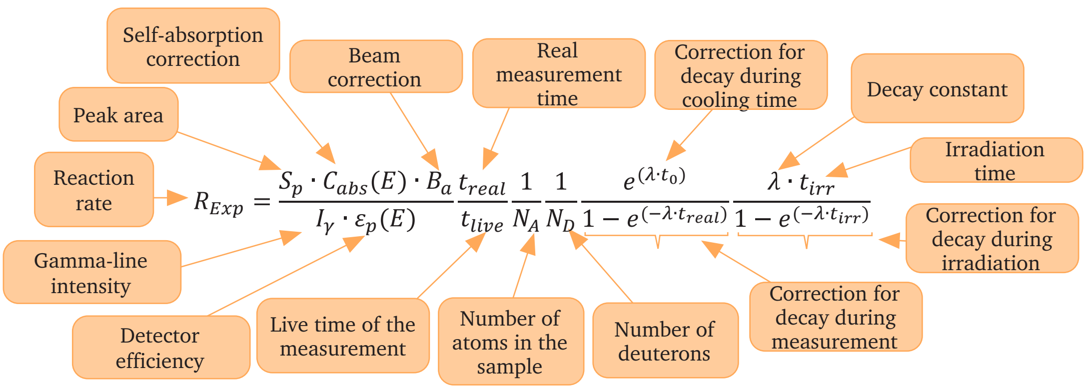

Figure 1. Reaction rate formula

Source: [9]

The effective cross-section of the reaction σ expresses the probability of this transformation in 1 s when the nucleus is bombarded with a flux density of 1 particle in 1 s per 1 cm^2. If N nuclei are contained in the target and the flux of I particles per 1 cm^2 per s falls on it, then σNI of nuclear transformations per 1 s occurs. The total effective cross section is the sum of the cross sections of the processes on all channels:

$$\sigma = \sigma_b + \sigma_c + \cdots \quad (3)$$

The reaction depends on the effective heat cross section of the incident particle, which is important:

$$\sigma = f(E) \quad (4)$$

In real physical experiments, it is not always possible to directly measure the effective cross section. The directly measured value is the yield of the reaction. The output of the nuclear reaction B at a given energy of the falling particles is the ratio of the number of acts of reaction that occurred to the number of particles that fell on the target, provided that all target nuclei fall the same stream of bombarding particles. The yield can be calculated if the known effective cross section of the process σ:

$$B = \frac{I_0 - I}{I_0} = \frac{I_0(1-e^{-\sigma n})}{I_0} = 1 - e^{-\sigma n} \approx \sigma n \quad (5)$$

For targets of complex isotopic composition and targets in which the studied isotope is part of a chemical compound, there is the following formula for calculating the cross section:

$$\sigma_a\left(E_\gamma(j)\right) = \frac{S_\gamma(E_\gamma(j))\lambda_a \mathrm{x} \frac{t_{r,i}}{t_{l,i}}}{N_p N_{targ} \varepsilon_\gamma I_\gamma\left(E_\gamma(j)\right)(1-e^{-\lambda_a \tau_1})e^{-\lambda_p t_{2,i}}(1-e^{-\lambda_a t_{r,i}})}, \quad (6)$$

$\lambda_a[c^{-1}]$ – is the decay constant for the nucleus a; $\varepsilon_\gamma(E_\gamma(j))$ absolute efficiency of registration of γ-quanta with energy $E_\gamma(j)$; $I_\gamma\left(E_\gamma(j)\right)$ – intensity of gamma ray decay with energy $E_\gamma(j)$;τ_1, t_2, $t_{r,i}$, $t_{l,i}$ – exposure time, delay, real and real measurement time, respectively.

The ratio between the cross sections of the daughter product and the main maternal product σ_a [10]:

$$S_\gamma(E_{\gamma,i}) = \{Ae^{-\lambda_a t_2(i)}\left(1 - e^{-\lambda_a t_{3,r}(i)}\right) + Be^{-\lambda_b t_2(i)}\left(1 - e^{-\lambda_b t_{3,r}(i)}\right)\}\frac{t_{3(l,i)}}{t_{3(r,i)}} \quad (7)$$

Experimental setup

The experiment was carried out at the Phasotron at the Joint Institute for Nuclear Research (JINR) in Dubna. The experiment is to irradiate a thin target composed of a mixture of PuO_2 with Al. Irradiation of the plutonium target occurred on the external proton beam with an energy of 660 MeV. The target was made according to the sandwich geometry of plutonium and aluminium product. The size of the object is Ø21x1.5 mm, it consists of ^{239}Pu foil, and its mass is 446 mg. At the same time, the thickness of the foil is about 58.1 microns. Three aluminium foils served as a monitor for the incident proton beam, and one as a collector of plutonium target fragmentation nuclides (Fig. 2).

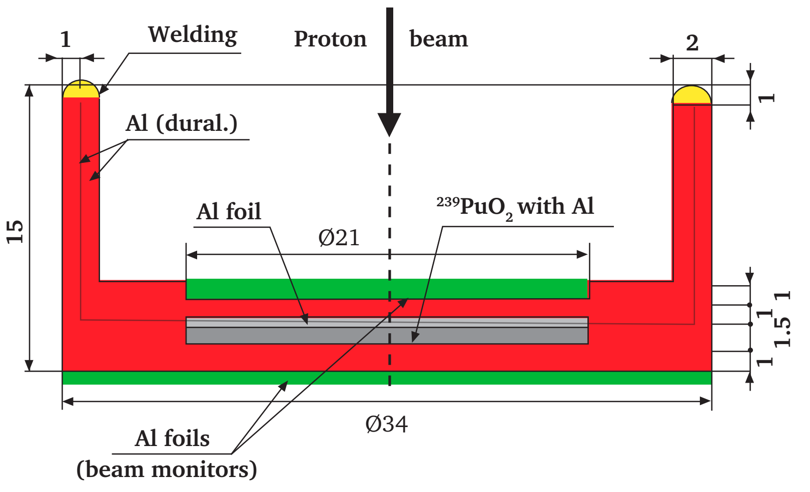

Figure 2. Arrangement and description of the plutonium target

Using Phasotron, the experimental samples were irradiated [11]. This device is a cyclic accelerator of heavy charged protons, which allows elements to carry out motor activity in a constant and uniform magnetic field, as well as to accelerate in a high-frequency electric field, which decreases in frequency. An accelerated series of protons provided an energy of 660 MeV. During the irradiation cycle, the tray with the sample sandwich inside was taped to the centre of a 50x50 mm, 0.1 mm thick aluminium plate placed on the fixture perpendicular to the protons. This position prevents the accumulation of ^{24}Na, ^{22}Na and ^{7}Be appearing on the Al monitor. All control over the intensity of the proton beam is provided by the monitor. Table 1 shows the exposure indicators of ^{239}Pu.

Table 1. Indicators of ^{239}Pu target irradiation

Energy, (MeV)	Mass of sample, (g)	Irradiation time, (min)	Integrated proton flux, p/(cm^2·s)x 10^{13}	Output beam current, mA
660	446	5.25	4.9 ± 0.1	2.02

Irradiation lasted 5.25 min; the experiment was performed after 12 minutes of experiment with Uranium. The integral flow of protons was (4.9 ± 0.1) 1013 as a result of starting a current of 2.02 mA in the output beam. The beam parameters are especially important for determination of the decay of short-lived nuclei during irradiation.

As a result of the irradiation, the objects were removed from the phasotron camera and placed on the spectroscopic mechanism of the YaSNPP-2. After that, the characteristic gamma radiation spectra of the released residual nuclei in the target were measured, in particular along the 1332 keV vector with a power of 19% and 1.78 keV of the CANBERRA HPGe detector. Due to the high activity of the sample, the irradiation was carried out at a great distance from the detector.

The transfer time of the plate to the detectors was not more than 10 minutes. The measuring position was chosen so that the dead time of the detector did not exceed 20%, and in the case of active samples did not reach much below 10%. As for actinides, which often have their own low-energy gamma particle, this use of the filter is very advantageous. Filters made of lead sheets provide the absorption of higher energies of gamma quanta. It is advisable to supplement them with filters with a smaller number of nucleons (Cd, Cu), which absorb X-rays excited in lead.

The study calculated the average proton flux density. With the help of activated aluminium films, the verification and control of the proton beam was implemented for the reactions ^{27}Al (p, 3pn) ^{24}Na, ^{27}Al (p, 3p3n+) ^{22}Na, ^{27}Al (p, 10p11n+)^{7}Be. A monitoring reaction was used for this purpose ^{27}Al (p, 3pn) ^{24}Na. Insights into the effective cross section on the Al plate reaction and their small energy dependence at high energies were used to monitor the number of protons trapped of the p + Al.

However, ^{27}Al (p, 3pn) ^{24}Na reaction is usually affected by the parasitic neutron reaction ^{27}Al (n, α) ^{24}Na. The effect depends on the distance of the aluminium foil from the system, and with a reasonable choice it is effect is in the order of units or tenths of a percent. Control can be carried out by reactions of ^{27}Al (p, 3p3n) ^{22}Na and ^{27}Al (p, 10p11n) ^{7}Be. When placing the film directly on the target, it can give these reactions 30% less proton integral (Table 2).

Table 2. The neutron- and proton-induced yields are calculated in the ratio of ^{24}Na, ^{22}Na and ^{7}Be formed in ^{27}Al+p

Degrader	Nuclide	$\overline{\sigma_n}$(mb)	σ_p (mb)	$\frac{N_n}{N_p}$	R (%)
Al	24Na	31.1	11.4	0.0301	8.21
	22Na	12.8	18.1		2.13
	7Be	0.0143	0.99		0.043

Source: [12]

Data calculation and evaluation

During the experiment, DEIMOS32 software was used for processing γ-spectra. DEIMOS32 software was developed at the Institute of Nuclear Physics in the Czech Republic (Rzezh) and at the Joint Institute for Nuclear Research in Dubna, was used to process γ-spectra [12]. Thanks to this software, it was possible to analyse and evaluate the peaks, their size and other indicators. In addition, an examination and detection of short-lived radionuclides formed in ^{239}Pu samples as a result of nuclear interaction with protons was carried out. The last process was implemented on the basis of a number of scripts belonging to the Ruby programming language (TimeConst, AttCor, EffCor, MidLit5, NonLin64, PureGam, SepDepe, SigmaJ7). The output files of each program in the package are input files for the next, and they must be in the root folder of the corresponding program, so the output files must be copied to the root of the program for which this file is input.

The study used the program EFEKT8.EXE, which determined the effectiveness of the HPGe detector. At high gamma radiation energy, annihilation radiation can leak out. After creating a positron-electron pair, the positron annihilates and creates two annihilation photons 511 keV. In germanium detectors, there is a high probability that one of the peaks of destruction will escape. If one of the photons escapes, one output peak (SEP) will appear in the measured spectrum. If both photons escape, a double output peak (DEP) will result.

The peak area of SEP or DEP can be determined according to the area of peak E at full energy:

$$S(E_{SEP}) = S(E_\gamma) * \epsilon_{SEP}(E_\gamma) \quad (8)$$

$$S(E_{DEP}) = S(E_\gamma) * \epsilon_{DEP}(E_\gamma) \quad (9)$$

ϵ_{SEP},ϵ_{DEP} are single and double-peak coefficients determined experimentally. These coefficients are independent of the distance of the target to the detector. The dependence of ϵ_{EP} on the peak energy is shown in the Figure 3.

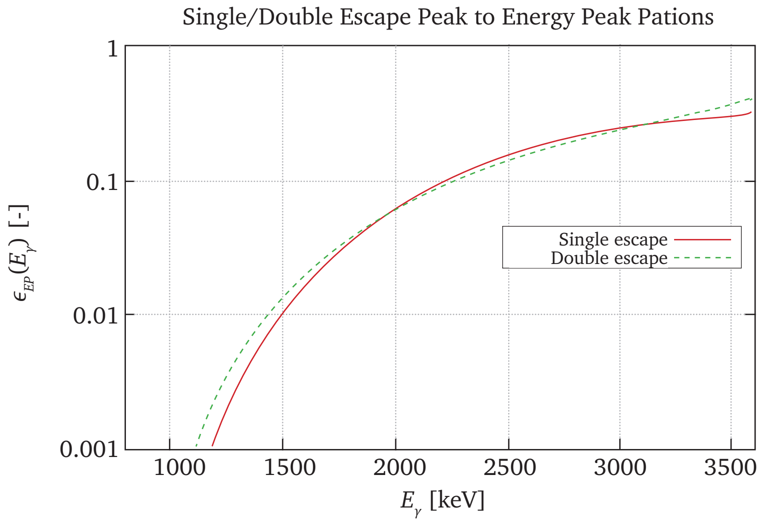

Figure 3. Experimentally determined dependency of SEP/DEP and full-peak area ratios on full-peak energy E_γ

Source: [13]

The parameters set by the program EFFEKT8 are given in the Table 3. The experimentally measured points were determined by formula:

$$\epsilon_{EP}(E_\gamma) = \exp\left(s_0 + s_1 * \ln(E_\gamma) + s_2 \ln(E_\gamma)^2 + s_3 \ln(E_\gamma)^3\right) \quad (10)$$

Table 3. Experimentally determined parameters $\epsilon_{EP}(E_\gamma)$ of the function

	SEP		DEP	
i	**Si [-]**	**ΔSi [-]**	**Si [-]**	**ΔSi [-]**
0	-2.0866027851	0.2860230743	-1.3273140355	0.1814312750
1	13.8832738535	1.1099975243	12.8053750577	0.8383854495
2	-8.2291578426	1.3992857931	-8.9129115117	1.1473203273
3	1.7178618884	0.5675750337	2.6470549618	0.4847393276

Source: [14]

The program that is responsible for correcting the efficiency of the detector. This amendment (η_e (E_γ)) is defined by the formula:

$$\eta_e(E_\gamma) = \exp\left(a_0 + \sum_{i=1}^{np} a_i ln^i(E_\gamma)\right) \quad (11)$$

a_i – parameters of the efficiency curve, estimated using the program EFFEKT8.EXE after a series of measurements calibration standards and E – gamma peak energy.

In the study AD4HEL – Activation Detectors for High Energy Lasers [15] program was used. This is a special program for the analysis of the spectrum of neutrons generated by the laser. Software developed on the basis of the Brno University of Technology, located in the Czech Republic. Only "prn" format is supported. This program gives possibility to calculate production/reaction rate: unit of production rate is the number of reactions in sample per 1 second and reaction rate is number of reactions normalised per one incident particle and one atom of foil (need integral flux). Some values and results are saved in the ".xlsx" file in the "out" folder.

Based on the energies of γ-rays Co-57, Eu-152, Co-60, Ra-226, Cd-109 and Ba-133, which have the required energy range, the quality (ε) of the structure of the HPGe detector was revealed. In parallel, the efficiency calibration can be performed in order to obtain not only the range of energy value but in the future also the values of the activity of the sample and radionuclide impurities. The change in the efficiency index with the heat of γ-radiation is not characterized by the location of the detector, although its absolute value is correlated with this feature.

Efficiency calibration: mathematical fitting 43 experimental values (points) in the 121-to-2614 keV range (Fig. 4). Fitting coefficients were determined for each position, which used to further calculate the result (Table 4).

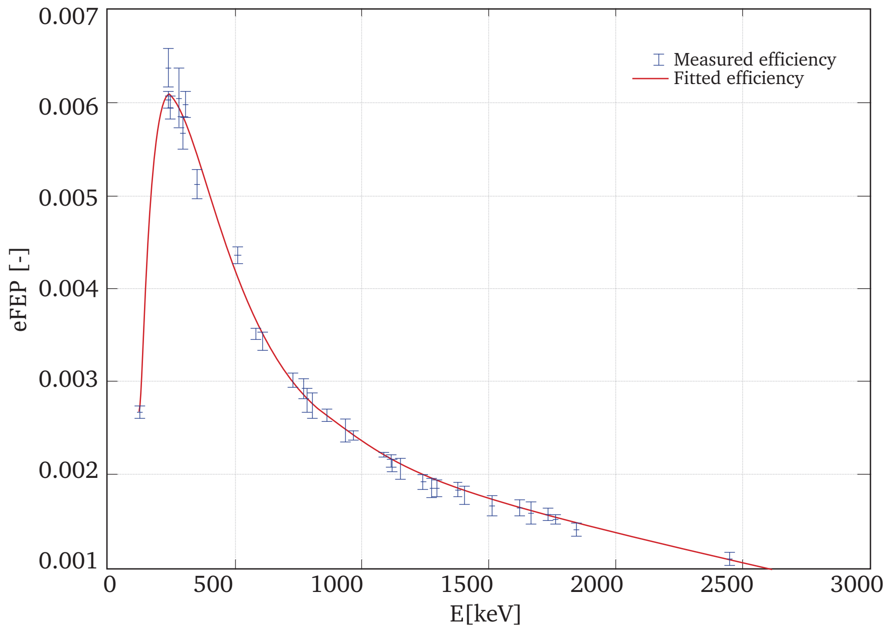

Figure 4. Efficiency calibration obtained with help of the Python scripts

Table 4. Efficiency fit coefficients of the HPGe-detector for example Position 2

a0	6.43425653
a1	-0.78928838
a2	0.09669678
a3	-0.20612789
a4	-0.440179361
a5	0.08561548
a6	0.25554557
a7	0.08057409

Results and Discussion

50 gamma lines and 31 nuclides (see Figs. 5, 6) were established as a result of the examination of 21 gamma spectra described for the irradiated plutonium target. During this process, the energy and half-life ranged from 14.4 m to 3.19 h. The investigated nuclides are characterized by indicators from 41-239 with gaps in indicators 41-149 and 197-239.A sample of ^{239}Pu was subjected to fragmentation during neutron irradiation. The latter was formed in an aluminium target. Quantitative materials for 31 nuclides were described with a wide range of plutonium fission elements:^{92}Sr, ^{89}Rb, ^{98m}Nb, ^{101}Mo, ^{95}Ru, ^{135m}Cs, ^{118m}Sb, ^{134}Te, ^{134}I, ^{130}La, ^{201}Bi and other. The results of isomers are shown in Table 5. All obtained nuclides are shown Figure 5-6. Also, ^{24}Na was obtained which formed in the aluminium foils.

Table 5. List of isomers with their cross-section

Isotope	E, keV	Iγ, %	RR, s^{-1}	dRR, s^{-1}	∑σ, b	dσ, b	$T_{1/2table,}$ h	$T_{1/2exp,}$ h
^{98m}Nb	722	73.8	2.63E-29	1.47E-30	2.33E-05	1.23E-06	0.85	1.56
	787	93	3.08E-29	1.64E-30			0.85	0.8
	1169	17.8	4.96E-30	3.25E-31			0.85	1.26
^{91m}Y	555	95	1.48E-29	1.34E-30	5.12E-05	2.36E-06	0.83	1.3
^{90m}Y	479		7.27E-30	3.67E-31	2.52E-05	9.79E-07	3.19	3.49
^{116m}In	1293	84.44	5.31E-29	2.79E-30	2.74E-05	7.31E-07	0.9	0.93
	1097	56.2	8.52E-30	4.50E-31			0.9	0.91
	2112	15.5	6.48E-30	4.33E-31			0.9	1.62
^{116m}Sb	843	11.2	1.08E-29	2.24E-30	4.15E-05	1.79E-06	1	0.16

Table 5, Continued

Isotope	E, keV	Iγ, %	RR, s^{-1}	dRR, s^{-1}	∑σ, b	dσ, b	$T_{1/2table,}$ h	$T_{1/2exp,}$ h
	1293	100	1.02E-28	1.27E-29			1	0.94
^{135m}Cs	846	95.9	3.37E-30	4.79E-31	1.79E-05	4.79E-07	0.88	0.67
	786	100	4.58E-30	1.83E-30			0.88	0.89
^{201m}Bi	846.833	5	1.77E-28	1.21E-29	9.87E-05	4.45E-06	0.98	1.33

Note: $\sum\sigma, b$ *– the sum of cross-section of all γ-lines for one isomer (b-barn)*

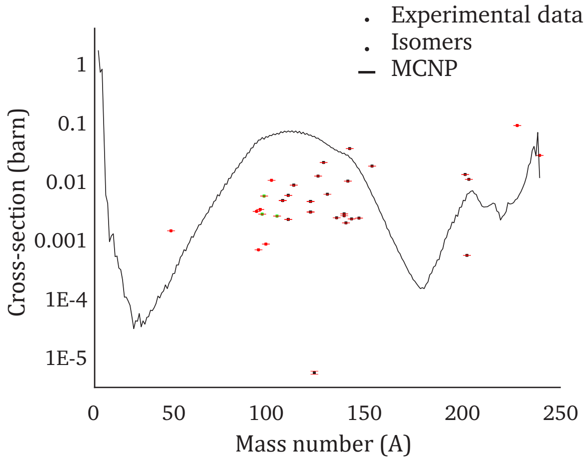

Figure 5. Calculated and experimental cross-sections of created isotopes in irradiated ^{239}Pu target

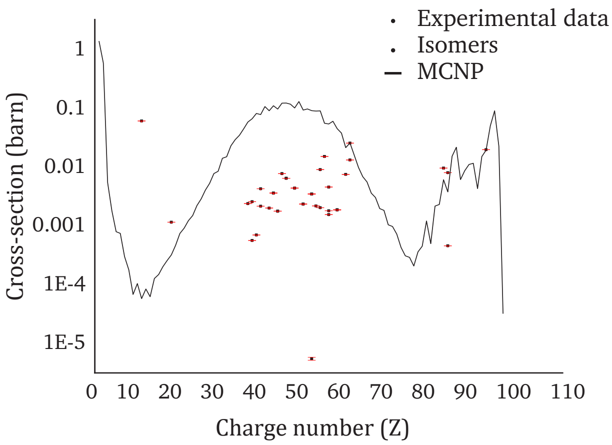

Figure 6. Calculated and experimental cross-sections of created isotopes in irradiated ^{239}Pu target

In Figures 5-6 the red points are experimental data, and the green points are obtained isomers. The figures reveal the researched and developed cross-sections of short-lived radionuclides that were identified in the ^{239}Pu target. The latter, in turn, was irradiated with a beam of 660 MeV protons.

As it was mentioned before, plutonium is widely used in the nuclear industry as a component for nuclear weapon, fuel for nuclear reactors, as well as an energy source for space devices. Therefore, the need for experimentation for the plutonium study, its behaviour in reaction time, such as nuclear fission, is increased.

Most of the heavier elements, such as plutonium, uranium and others, fission under the influence of protons, if the proton energy is high enough to overcome the nucleus Coulomb repulsion. In the work carried out, the plutonium target was bombarded with a number of protons characterized by an energy of 660 MeV. As a result of the conducted research, it was possible to establish 50 gamma-lines and reveal 31 nuclides, the obtained results are confirmed by the data presented in the previous section.

In order to compare the obtained research results, their confirmation or refutation, an analysis of works in this field by other authors over the last few years of publication was carried out. Since the reaction of nuclear fission belongs to multifaceted cycles, which are affected by a number of indicators, therefore a rather small number of works have been covered in this area.

In their study, J. Adam et al. [16] studied the transmutation of ^{238}Pu and ^{239}Pu and other radioactive chemical elements such as ^{129}I, ^{237}Np, and ^{241}Am. During the work, the “Energy and Transmutation” target was irradiated with a number of protons. In turn, the latter were formed from the Nuclotron accelerator. The research was conducted in russia, namely at the High Energy Physics Laboratory of the Joint Institute for Nuclear Research in Dubna. In the neutron field, outside the blanket, and the outputs of transmutation reactions (the outputs of the formation of residual nuclei) were determined using γ-spectroscopy, it was possible to irradiate samples of radioactive iodine, neptunium, plutonium, and americium. An examination of the energy distribution of the neutron field was carried out, based on a number of threshold detectors. According to the authors, the results of this scientific work are among the primary indicators of plutonium transmutation in the “Energy and Transmutation” target-blanket system. According to the work results, ^{238}Pu has a smaller fission cross-section than ^{239}Pu in the energy region below 0.5 MeV. Five ^{238}Pu fission products and 19 ^{239}Pu fission products are observed.

Another work by J.-S. Wang et al. [17] was aimed at researching transmutation. In this work, the transmutation of ^{239}Pu and similar differentiated elements ^{91}Sr, ^{92}Sr, ^{97}Zr, ^{99}Mo, ^{103}Ru, ^{105}Ru, ^{129}Sb, ^{132}Te, ^{133}I, ^{135}I and ^{143}Ce was investigated. The research was conducted on the basis of the Joint Institute for Nuclear Research in Dubna. For a beam of protons, the energy of which corresponds to 1.0 GeV, the differentiation dynamics of ^{239}Pu was 0.0032 atoms per proton in plutonium samples weighing 1 g; for a proton with an energy of 0.53 GeV is about 0.0022. The studied error can reach 15%. Surveys are analysed and evaluated based on the numerical data of a pair of theoretical models with negligible efficiency with the implementation of the Duben Cascade Model (CEM) and the LAHET code.

A. Al-Adili et al. [18] in their work studied the effect of corrections for prompt neutrons on the final fission fragments distributions. According to the authors, the multiplicity of fast neutrons also depends on the weight of the fragment and the kinetic energy of fragmentation. These indicators are characteristic of a small number of fission reactions under the influence of thermal neutrons. As a result of their study, the authors concluded that establishing an approach to neutron operations played an important role in the context of the nature and planning of the differentiation reaction. In this way, it affects the formation of new surveys that concern the calculations of fission fragments, which are more similar to fission neutrons. In addition, the qualitative analysis of the output of post-neutron fragments affects the correct assessment of the processing of nuclear surplus products and the effective selection of methods for the output of precursors of late neutrons.

J.P. Lestone [19] developed the interpolation method between and/or extrapolation from two fission product yield curves to the first chance neutron emission of mass-asymmetric fission. Measured spontaneous fission of ^{240}Pu, as well as thermal neutron fission of ^{239}Pu fission element excesses (FPY) are determined to establish the probable energy interaction and n + ^{239}Pu FPY for incident neutron characteristics from 0 to 16 MeV. As a result, the inclusion of innovations related to mass-symmetric differentiation, neutron emission, and multi-hour fission revealed by the FPY model are described with the data and estimate of ENDF/B-VII.1. In addition, the model is provided with the ability to reproduce the energy dependence of the ENDF/B-VII.1 estimate, indicating that the weight classification of differentiated plutonium is not fixed on the plane of the fission barrier, but is characterized by heat and surface nuclear potential energy, especially during significant changes.

Research by D. Neudecker et al. [20] was aimed at evaluating the energy spectra of neutrons emitted instantaneously as a result of the differentiation of ^{235}U and ^{239}Pu. Neutron energy spectra were reanalysed for ENDF/B-VIII.0. Complementing the considered data, which is published and characteristic of ENDF/B-VII.1, relevant surveys are disclosed in the context of experimental specific indicators or concerning a number of properties of incident energy, materials on deformed measurements that reveal differences. In addition, the factors affecting the size and distribution of the total kinetic energy from the energy tasks of the incident neutron were determined. The considered and proven numerical materials and covariances fully correspond to the studied amount of information that affects the conduct of the survey and the establishment of the assessment.

M. Alrwashdeh [21] analyzed ^{239}Pu based on the SAMMY code for neutron operations in the resonance plane up to 2.5 keV. In state 8.0.0 of the SAMMY code, the handling of wide covariance matrices of opposite parameters was developed. The value of this article lies in the analysis of the investigated information using the specially formed fitting code of the studied nuclear materials FITWR and their analysis using the SAMMY code, as well as the evaluation of indicators with the Bayesian approach. The output of these methods is based on the SAMMY code, in order to reveal the opposite parameters of the covariance matrix within the range of energies from 0 to 2.5 keV. Thus, the experiments conducted within this paper were conducted at the IMAN1 facility, the Jordan National Supercomputing Centre (IMAN1).

As it can be seen from the literature analysis, most of the work was aimed at studying the transmutation of ^{239}Pu, while in the carried out experimental work the main vector was aimed at studying the reaction of fragmentation and fission of the ^{239}Pu nucleus at an energy of 660 MeV. Nuclear fission, fragmentation and transmutation are interrelated processes. The key difference between these concepts is that fission is the process of nuclear fission, fragmentation is the process of ions dissociation from molecules, and transmutation is the process of transformation of one nucleus into another, as a result of nuclear reactions. The study of the radioactive element behaviour in induced processes is a very important part of the experiments.

In comparison with previous studies, it can be emphasised that this work confirms the results obtained earlier. It can also be noted that this work complements the previous study and is exclusive in its kind.

The next logical step in conducting experimental work is the search for primary products (mother cores) and the evaluation of the received information in accordance with computer modelling materials. Also, it will be very important to conduct a study on the study of plutonium fission under the influence of deuterons, or under the action of slow neutrons.

Conclusions

In this experiment, the reactions of fragmentation and fission of the ^{239}Pu nucleus at the energy of 660 MeV were investigated. The experiment focuses on the determination of short-lived radionuclides. Irradiation of the sample took place on a direct proton beam by means of activation gamma spectrometry and so-called direct kinematics. This measurement method has been used for a long time for very accurate and complete measurement of the effective cross sections of nuclear reaction nuclei under special conditions, namely high heat. When measuring the qualitative distribution of the exploitation of protons with ^{239}Pu nuclei by γ-spectroscopy and mass spectrometry methods, the arrival of protons into the plutonium target is detected, after which residual products are formed that stop in the target.

In total, 85 spectra were measured as a result of the experiment. The survey and calculations were carried out on different planes based on two HPGe detectors from CANBERRA and ORTEC, the efficiency of which is from 19% to 33%, and the resolution is from 1.78 keV to 1.86 keV along the 1332 keV line. The calculations were divided into two parts (1-5 positions by CANBERRA detector, 6-9 positions by ORTEC detector) to avoid overlap of energy lines, accurate identification of radionuclides, and due to different characteristics of the used detectors (efficiency, nonlinearity, etc.). For a complete picture of the formed radionuclides, it is necessary to calculate the results separately.

Therefore, as a result of the examination of 21 gamma spectra calculated by the Canberra detector, during the study of the plutonium target that was irradiated, 31 nuclides were identified, for which the reaction rate and effective cross sections were determined. Figure 5-6 shows the results of effective cross-sections of the spallation products of the plutonium target. These data can serve as input data for theoretical simulations of the interaction of protons with ^{239}Pu, and they can be a supplement to the nuclear database. The study is useful for future applications of accelerated nuclear waste transmutation and energy enhancement (subcritical type reactor). The obtained experimental result is compared with the simulation on MCNP 6.1 (Fig. 5-6). The data overall correspond to the expected range but for a complete result needs to be evaluated other spectres. The logical next step is to search for primary products (mother nuclei) and compare the obtained experimental data with the results of computer simulations (Geant4, MCNP or other).

References

[1] Carminati F, Klapisch R, Revol JP, Roche Ch, Rubio JA, Rubbia C. 1993. An energy amplifier for cleaner and inexhaustible nuclear energy production driven by a particle beam accelerator [Internet]. Available from: https://cds.cern.ch/record/256520/files/at-93-047.

[2] Rubbia C, Rubio JA, Buono S, Carminati F, Fietier N, Galvez J, et al. 1995. Conceptual design of a fast neutron operated high power energy amplifier [Internet]. Available from: https://www.oecd-nea.org/trw/docs/rubbia/concept.pdf.

[3] Venneri F, Bowman CD, Williamson MA, Ning L, Bhatia TS, Jensen RJ, et al. Accelerator-driven transmutation of nuclear waste: Status, new concepts and future development. New Mexico: Los Alamos National Laboratory; 1996.

[4] Takizuka T, Nishida T, Sasa T, Takada H, Meigo S, Mizumoto M, et al. Fuel Cycle Systems. In: Proceedings International Conference on Evaluation of Emerging Nuclear; 1995. Versailles. Versailles: Nuclear Energy Agency; 1995. P. 489-96.

[5] Bátěk D. Nuclear reactor fuels and the fuel cycle. Brno: Vysoké Učení Technické v Brně; 2010.

[6] Kebin EI. 2016. Nuclear power [Internet]. Available from: http://nuclphys.sinp.msu.ru/ne/.

[7] Titarenko YuE, Shvedov OV, Igumnov MM, Michel R, Mashnik SG, Karpikhin EI, et al. Experimental and computer simulation study of the radionuclides produced in thin ^{209}Bi targets by 130 MeV and 1.5 GeV proton-induced reactions. *Nucl. Instrum. Methods Phys. Res.* 1998;(414):73-99.

[8] Michel R, Bodemann R, Busemann H, Daunke R, Gloris M, Lange HJ, et al. Cross sections for the production of residual nuclides by low- and medium-energy protons from the target elements C, N, O, Mg, Al, Si, Ca, Ti, V, Mn, Fe, Co, Ni, Cu, Sr, Y, Zr, Nb, Ba and Au. *Nucl. Instrum. Methods Phys. Res.* 1997;(129):153-93.

[9] Zeman M, Adam J, Baldin AA, Chilap VV, Furman WI, Katovsky K, et al. 2020. Reaction rates of residual nuclei produced of 59Co at the target QUINTA. [Internet]. Available from: https://pos.sissa.it/225/061/pdf.

[10] Adam J, Mrazek J, Frana J, Pronskikh VS, Kalinnikov VG, Priemyshev AN, et al. Program package and supplements to activation analysis for calculations of nuclear reaction cross sections. *Meas. Tech*. 2000;(1):1-22.

[11] Onischenko LM. JINR phasotron. In: 12th IEEE Particle Accelerator Conference; 1987. New York. New York: IEEE; 1987. P. 878-82.

[12] Szelecsényia F, Steyn GF, Nortier FM, Kovács Z. New cross sections for the ^{27}Al (p, x) ^{7}Be nuclear process: Monitoring proton beam energy via the $^{22}Na/^{7}Be$ cross-section ratio between 45 and 200MeV. *EPJ Web Conf.* 2017;(146):1-4.

[13] Frána J. Program DEIMOS32 for gamma-ray spectra evaluation. *J. Radioanal. Nucl. Chem*. 2003;(257):583-7.

[14] Adam IB, Kalinnikov VG, Pronskikh VS, Adam II, Gonusek M., Gromov KYa. Analysis of complex γ-radiation spectra. Gatchina: PIYaF; 1998.

[15] AD4HEL – Activation detectors for high energy lasers: Využití kvasi-offline metod pro detekci laserem generovaných neutronů. 2019-2021 [Internet]. Available from: https://www.vut.cz/en/rad/projects/detail/30357.

[16] Adam J, Katovsky K, Balabekyan A, Kalinnikov VG, Krivopustov MI, Kumawat H, et al. Transmutation of ^{129}I, ^{237}Np, ^{238}Pu, ^{239}Pu, and ^{241}Am using neutrons produced in target-blanket system 'Energy plus Transmutation' by relativistic protons. *Pramana.* 2007;(68):201-12.
[17] Wan J-S, Langrock E-J, Westmeier W, Vater P, Brandt R, Adam J, et al. Transmutation of Pu-239 with spallation neutrons. *J. Radioanal. Nucl. Chem*. 2001;(247):151-7.
[18] Al-Adili A, Hambsch F, Pomp S, Oberstedt S. Impact of prompt-neutron corrections on final fission-fragment distributions. *Phys. Rev. C.* 2012;86(5):article number 054601.
[19] Lestone JP. Energy dependence of plutonium fission-product yields. *Nucl. Data Sheets*. 2011; 112(12):3120-34.
[20] Neudecker D, Talou P, Kawano T, Kahler AC, White MC, Taddeucci TN, et al. Evaluations of energy spectra of neutrons emitted promptly in neutron-induced fission of 235U and 239Pu. *Nucl. Data Sheets*, 2018;(148):293-311.
[21] Alrwashdeh M. ^{239}Pu evaluation comparison study. *Ann. Nucl. Energy*. 2018;(118):313-6.

Дослідження реакції спаляції на плутонієвій мішені, опроміненої протонами з енергією 660 МеВ

Ангеліна Миколаївна Танчак[1], Карел Карелович Катовський[2], Іван Іванович Гайсак[3], Їндріх Їндріхович Адам[4], Роберт Робертович Голомб[5]

[1]аспірант, ORCID: https://orcid.org/0000-0001-6566-7007.
Технологічний університет у Брно, 60190, вул. Антонінська, 548/1, Брно, Чеська Республіка
[2]кандидат технічних наук, доцент, ORCID: https://orcid.org/0000-0001-9335-8199.
Технологічний університет у Брно, 60190, вул. Антонінська, 548/1, Брно, Чеська Республіка
[3]кандидат фізико-математичних наук, ORCID: https://orcid.org/0000-0003-4643-187X.
Ужгородський національний університет, 88000, пл. Народна, 3, м. Ужгород, Україна
[4]кандидат технічних наук, ORCID: 0000-0002-9850-7007.
Технологічний університет у Брно, 60190, вул. Антонінська, 548/1, м. Брно, Чеська Республіка
[5]Аспірант, ORCID: https://orcid.org/0000-0001-7918-7581.
Технологічний університет у Брно, 60190, Антонінська 548/1, Брно, Чеська Республіка

Анотація

Актуальність. У статті описано вимірювання перерізів реакцій поділу та відколу плутонієвої мішені, опроміненої протонним пучком з енергією 660 МеВ на прискорювачі Фазотрон Об'єднаного інституту ядерних досліджень.

Мета. Експеримент спрямований на визначення короткоживучих радіонуклідів.

Методологія. Експериментальний зразок вимірювали в автономному режимі за допомогою гамма-спектрометрії з HPGe детектором. Досліджено швидкості реакцій утворених залишкових ядер. За допомогою методу прямої кінематики визначали продукти реакції відколу. Для обробки γ-спектрів використовували програмне забезпечення DEIMOS32. За допомогою програмного забезпечення TJ02000321–V3 було ідентифіковано ядра, що утворилися в зразку ^{239}Pu в результаті ядерних реакцій з протонами. Продукти реакції були ідентифіковані на основі гамма-енергій, інтенсивності та періоду напіврозпаду після вимірювання.

Результати. У результаті обробки гамма-спектрів, виміряних для опроміненої плутонієвої мішені, було виявлено 50 гамма-ліній, а 31 нукліди ідентифіковані за енергією та періодами напіврозпаду від 14,4 м до 3,19 год. Виміряні перерізи ядерних реакцій можуть слугувати опорними даними для теоретичного моделювання взаємодії протонів з ^{239}Pu і можуть бути доповненням до ядерних баз даних.

Висновки. Отриманий результат експерименту порівнюється з моделюванням на MCNP 6.1. Загалом отримані дані відповідають очікуваному діапазону, але дані все ще потребують додаткової оцінки. Наступним логічним кроком є пошук первинних продуктів (материнських ядер) та порівняння отриманих експериментальних даних з результатами комп'ютерного моделювання

Ключові слова: фазотронний прискорювач, програмне забезпечення TJ02000321–V3, гамма-спектри, радіонукліди, γ-спектроскопія, системи з прискорювачем

Scientific Herald of Uzhhorod University
Series "Physics"

Journal homepage: https://physics.uz.ua/en
Issue 52, 46-55
Received: 10/20/2022. Revised: 12/01/2022. Accepted: 12/19/2022

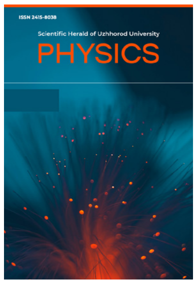

UDC 669.1:620.1
PACS 81.05.Bx, 81.40.–z
DOI: 10.54919/2415-8038.2022.52.46-55

Study of hardening and structure of maraging powder steel grade PS-H18K9M5TR (18%Ni+9%Co+5%Mo+1%Ti+1%Re+66%Fe)

Suren Aghbalyan[1*], Vigen Simonyan[2]

[1]Full Doctor in Technical Sciences, Professor. ORCID: https://orcid.org/0000-0001-9987-8515.
National Polytechnic University of Armenia,
0009, 105 Teryan Str., Yerevan, Republic of Armenia

[2]Graduate Student. ORCID: https://orcid.org/0000-0002-9293-0955.
National Polytechnic University of Armenia,
0009, 105 Teryan Str., Yerevan, Republic of Armenia

Abstract

Relevance. High-strength steels are increasingly in demand in modern industry for various applications. Maraging steels are the primary material in the manufacture of most aircraft parts as well as machine-building components. This type is low-carbon and is rich in nickel, which forms martensite when cooled as well as demonstrates properties such as high hardness, wear resistance, etc. The hardening process is the main factor affecting the functional properties of maraging steel. At certain temperatures, austenite has the ability to transform into various kinds of phases. However, the shortcoming that lies in the presence of some impurities limits the established types of improvement technologies, leading to the search for innovative methods to improve the characteristics of steel without losing any of the desired properties. Good qualities appear in maraging steels mainly after treatment with a solution at a temperature of about 1000°C and during aging at a temperature of about 490°C.

Purpose. Thus, the purpose of this research paper is to analyze the structure of maraging steel powders and study the thermal effect on its properties.

Methodology. In this paper, powder steel was pressed by spark plasma sintering technology at a pressure of 60 MPa to a powder compact and heated at a temperature of 1100°C for 180 s at a rate of 20°C/s, after which the samples underwent phase and elemental analysis, their hardness was measured, the value of which amounted to about 60 HRC.

Results. The results of this scientific research demonstrate the presence of a variety of precipitates. The presence of impurities such as Co, Ti, and Re led to an improvement in strength due to martensitic phase transformation and precipitation hardening, as well as slowed down the diffusion process.

Conclusions. In addition, tasks for further research on the issue of manufacturing maraging steels by the additive manufacturing method were identified. This technology enables obtaining strong maraging steels based on a powder mixture with the required characteristics

Keywords: spark plasma sintering, laser processing, additive manufacturing, heavy-duty steel, heat treatment

Suggested Citation:
Aghbalyan S, Simonyan V. Study of hardening and structure of maraging powder steel grade PS-H18K9M5TR (18%Ni+9% Co+5%Mo+1%Ti+1%Re+66%Fe). *Scientific Herald of Uzhhorod University. Series "Physics"*. 2022;(52):46-55.

*Corresponding author

Introduction

Various branches of engineering require the refinement of high-strength steels. Maraging steels are low-carbon high-strength steels. Their structure and characteristics with good mechanical properties provide resistance to impact loads. High-alloy maraging steels with high strength and processability as well as good fracture toughness are popular in various areas of activities (for example, in the aerospace industry, mechanical engineering, various types of structures) [1; 2]. Despite the low carbon content, high strength values are due to the Ni-martensitic matrix as well as the presence of significant dislocation density, subsequently formed martensitic metamorphosis, atoms of a chemical compound between elements in the form of a phase of variable composition or intermetallic compound. The deposition of such compounds is one of the most effective ways of hardening maraging steels. However, it should be emphasized that the high percentage of Ni with the combined presence of retained austenite sharply decreases the steel's strength. Ni is an element that is widely used as an impurity, with Mo, Cu, Ti and others following it. During aging, the metastable state has an increased free energy, and therefore tends to decay with deposition of phases that give strength: Fe_2Mo, Ni_3Ti (Mo), etc. An increase in the content of impurities of various kinds leads to an increase in the volume of precipitated phases and greater dispersion strengthening, despite the fact that a shortage of such elements leads to the search for new ways to improve the functional characteristics of steels without losing such properties as ductility, brittleness and toughness.

At high temperatures, Fe has a face-centered cubic lattice (FCC), while at low temperatures it has a body-centered cubic lattice (BCC). A feature of maraging steels is martensitic hardening, i.e., intermetallic compounds are deposited in Fe-Ni martensite with negligible carbon content during aging, which hardens the steel. As reported by L.F. Van Swam, R.M. Pelloux & N.J. Grant [3], such steel is typically heat-treated using a one-hour solution annealing at 820°C followed by cooling to room temperature to form Fe-Ni martensite. The results of the maraging steel research by T.A. Chernyshova & T.V. Lyulkina [4] show that rapid hardening of maraging steels significantly affects the nature of phase metamorphoses, structure and functional characteristics of steels. Z.-F. Hu & Ch.-Xu. Wang [5] report grain refinement after heat treatment. However, hardness tests show that the mechanical properties of maraging steel do not depend significantly on grain size. Thus, the preparation of the austenitic phase in the martensitic matrix has a beneficial effect on the strength and ductility of the steel. In their paper, J.M. Pardal, S.S.M Tavares, V.F. Terra, M.R. da Silva & D.R. dos Santos [6] propose a model for the aging of maraging steel within the temperature range of 440-560°C using the following equation:

$$\Delta H = (kt)^n \tag{1}$$

where: k is the rate constant depending on temperature; n is the exponent that is weakly dependent on temperature; ΔH is the increase in hardening volume; t is the aging time.

In detail, the hardening process consists of quenching and aging, or of quenching, cold working and natural aging. Higher strength properties are achieved through hardening, deformation and aging [7]. During rapid quenching, a martensitic transformation occurs due to the shift of FCC to BCC, creating a microstructure with a high density of internal defects. When a quenched supersaturated solid solution is reheated to a certain temperature, the precipitates are formed and their number increase [8]. Morphology, dimensions and concentration of precipitates mainly depend on the chemical composition and hardening. It is worth to consider cases of lattice mismatch, which will lead to the formation of precipitates in the dislocation regions, which in turn weakens the ability to distribute precipitates throughout the matrix. In addition, there is the potential to regulate the concentration and number of precipitates by adjusting the solution treatment conditions [9].

Research journals lack information about the study of powders obtained by spark plasma sintering. Therefore, the purpose of this research is to study the structure after sintering of a maraging powder mixture and to analyze the heat treatment on its properties.

Materials and Methods

Maraging powder steel containing 18% Ni, 9% Co, 5% Mo, 1% Ti, 1% Re was selected the object of study. This steel belongs to class C maraging steel, which usually contains about 18% Ni as well as contains alloying elements such as Co, Mo and Ti. Powders are obtained by gas atomization, which is a polarization method for the production of powder steel. When sprayed, spherical particles with a relatively round shape are usually formed. As part of this process, the assimilation of the alloy occurs, which is subsequently excited by a gas flow at an ultrahigh speed. In the course of this, the liquid metal is distributed into droplets with further solidification in the form of continuous powder grains. The method for pressing powder mixture in this paper is the technology of spark plasma sintering by applying 60 MPa to the powder compact and heating it at a temperature of 1100°C for 180 s at a rate of 20°C/s. This method was chosen due to good compaction as well as high relative density. Figure 1 shows a schematic representation of the SPS (spark plasma sintering) technology unit, which includes graphite molds, into which the powder mixture is poured between stampings. An image of the powder mixture is shown in Figure 2, 3 shows sintering results.

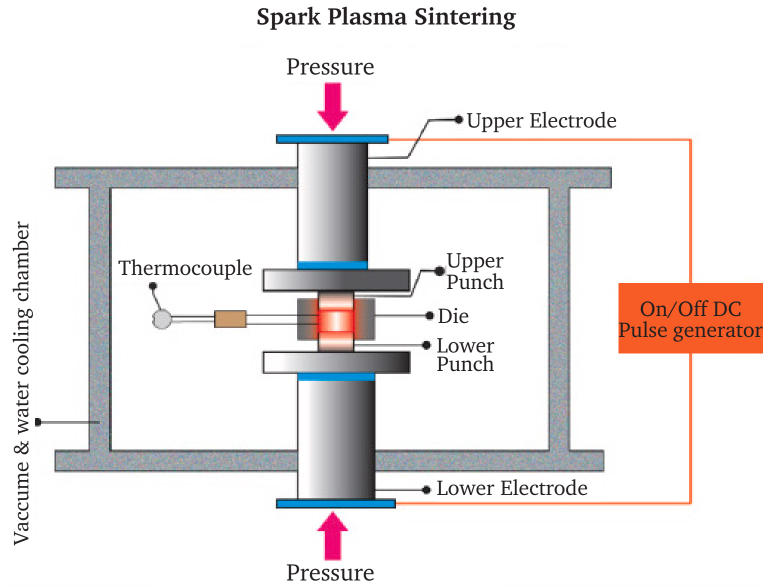

Figure 1. SPS technology unit diagram

Source: [10]

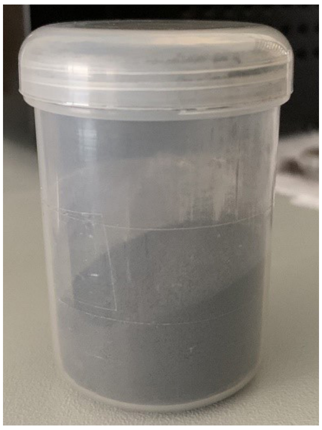

Figure 2. Image of the powder mixture before sintering

Figure 3. Image of powdered steel after sintering

To study the microstructure before observation, the samples were etched in a Fry's reagent solution ($FeCl_3$ + $CuCl_2$ + HNO_3 + HCl + ethanol + H_2O) and then examined using scanning electron microscopy (SEM). To study the characteristics, a Difrey-401 diffractometer was used to obtain phase and elemental analysis. The phases are established by comparing and matching the diffraction angles and intensity values of the diffraction peaks with well-known template X-ray patterns obtained from open sources. In the cubic system, the a_{hkl} lattice parameter for diffraction from (*h*, *k*, *l*) defined by the diffraction angle θ_{hkl} is calculated as follows:

$$a_{hkl} = \frac{(h^2+k^2+l^2)^{1/2}}{\lambda/2sin\theta_{hkl}} \quad (2)$$

where: λ is the X-ray wavelength.

The share of austenite in the linear model varies depending on temperature, ranging from the beginning and end of austenite occurrence (617°C and 674°C respectively). The transformation of austenite to martensite is calculated using the Koistinen-Marburger phase transformation model:

$$f_{martensite} = f_{austenite}[1 - \exp(-0.011(M_s - T)) \quad (3)$$

where: *f* is the volume fraction of the phase; *Ms* is the initial temperature, at which martensite appears.

The following section is divided into three main parts, which discuss important aspects for this research. To begin with, the issue of the hardening effect on the structure and functional characteristics of martensite-containing steels was considered. For comparison, studies are given where the authors carried out different types of heat treatment of steels, the microstructure, phase transformations and properties of which were subsequently considered. The second part analyzed an innovative method for the production of maraging steels using laser technologies for powder mixtures. The results of the influence on the structure and properties of steels produced using this technology are presented. The third part analyzes the effect of chemical composition on the structure and mechanical properties of maraging steels. The research papers cited as examples can be used as a basis for further research.

Results and Discussion

Below are the sampling areas of initial powder and sintered powder steel (Fig. 4). The data obtained, presented in Table 1, confirm the composition of the powder mixture.

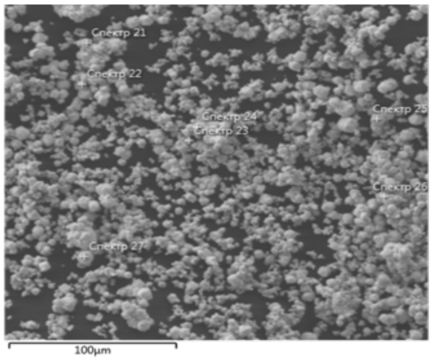

Figure 4. Selective sampling region

Table 1. Elemental analysis of the initial powder

Spectrum number	Element content, atomic fraction, %					
	Fe	Ni	Co	Mo	Ti	Re
1	67	15	8	7	1	1
2	68	13	6	4	1.3	0.8
3	69	18	9	3	1.5	0.9
4	61	20	4	4	0.9	0.7
5	62	18	8	5	0.85	1.2
6	64	19	9	6	0.9	1.1
7	63	18	10	3	1.1	0.95
8	66	17	7	5	1.2	0.9

During phase analysis, it was noticed that diffusion reactions slowdown, which in turn affects the formation of phase inhomogeneity throughout the volume of the material obtained. The Rockwell hardness of the samples was also measured, the value of which amounted to 60 HRC.

Martensitic transformation theories provide specific parameters for each of the geometric and crystallographic features of the transformations assigned to a particular invariant shift system. That is, each variant of the correspondence between the lattice and its orientation is the result of the choice of an invariant lattice shift system. The high strength of maraging steels was achieved due to the martensitic $\gamma \rightarrow \alpha$ transformation and martensite aging. The fatigue properties of the material are explained by its service life. That is, these properties are usually qualified as the ultimate performance indicator that determines whether a material can be developed for further use. The experiments performed show the possibility of forming structures such as martensite, ferrite, a chemical compound of martensite and ferrite-forming elements, such as oxyfer, depending on the rate of cooling of solid solution and subsequent cooling. The formation of an austenite phase at the boundary of a martensite grain plays a significant role in reducing the concentration of deformation stresses and coordinating deformation. Part of the austenite phase was retained during quenching. The maximum amount of reduced austenite is mainly observed at room temperature. The aging of the steel under study is accompanied by the formation of intermetallic compounds such as $Fe_3(Ni, Mo)$, Fe_2Mo, FeMo, Ni_3Ti, Ni_3Mo, ŋ-Ni_3Ti, as well as Fe_7Mo_6. That is, such compounds increase strength by accompanying the formation of segregations, metastable and stable phases, but with a sharp decrease in ductility. The sintered powder steel in the annealed state has a fully martensitic structure.

J. Tian, W. Wang, H. Li, M. Babar Shahzad, Y. Shan, Zh. Jiang & K Yang [11] talk about a method to increase the hardness of maraging steel by quenching. J.M. Pardal, S.S.M Tavares, V.F. Terra, M.R. da Silva & D.R. dos Santos [6] report that direct aging provides the stiffest state with the highest flexural strength. There are also opinions about improving the microstructure due to the transformation of martensite into austenite using thermal cycling. The distribution of elements after thermal cycling accelerates the kinetics of formation and growth of austenite grains. The transformation of martensite into austenite depends on diffusion phenomena occurring within a certain temperature range. Therefore, the stimulation of metamorphosis in the temperature range where sedimentary phenomena are not observed and the stabilization of reverse austenite at room temperature is of paramount importance for improving the functional properties of the steel. Based on the data obtained from elemental analysis, it is possible to identify an area enriched in iron, i.e., the basis of the compressed powder mixture (Fig. 5) is an iron frame. Elemental analysis also shows that in the range of at least 26 microns, there is a large amount of iron on the surface with added alloying elements. The micrographs of the samples (Fig. 6) show a small porous structure formed after sintering. In addition to the main particles, there are fractions of regular spherical shape, located mainly at the junction of large Fe grains. The shape and arrangement of the particles of this fraction allows assuming that they were formed due to the liquid phase. It should also be noted that their size does not exceed the size of small pores.

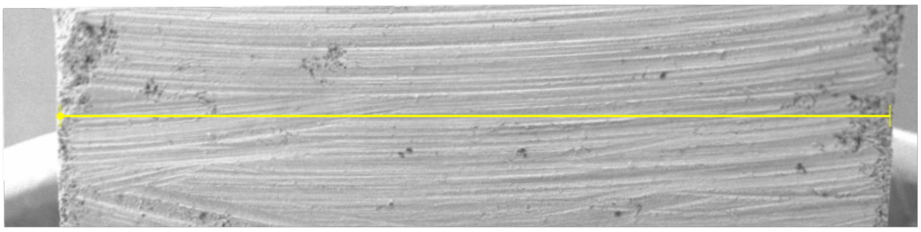

Figure 5. Image of a cut of pressed powder steel

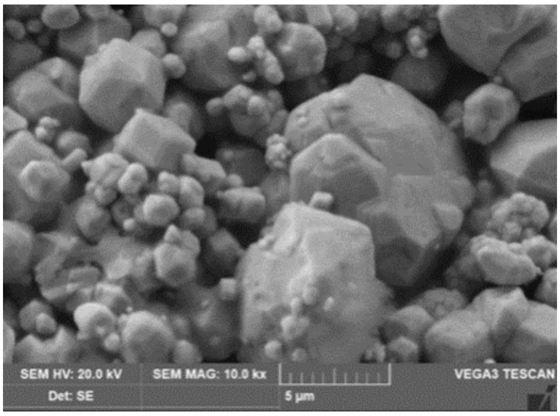

Figure 6. Sample micrography

Thus, the basis of the microstructure of the hardened 18% maraging steel is martensite with a low carbon content and a high content of nickel and cobalt. Aging at low temperatures (<450°C) occurs due to ordered and coherent phases, and will also be followed by the propagation of dislocations, which play an important role in increasing hardness and strength during aging. However, the propagation of dislocations can lead to the appearance of precipitates, such as Ni_3Ti (Mo), and an increase in their concentration. Hardening at high temperatures (above 850°C) leads to the increase in grain size and ductility. Therefore, it is necessary to harden maraging steels at 800-850°C in air, followed by aging within the temperature range from 480°C to 520°C.

A detailed analysis of the steel microstructure is the most important indicator in describing the material for the correct definition of purpose and application. Also, mechanical properties directly depend on the nature and features of the microstructure. The chemical composition can affect the change in phase stability. Alloying powder steel with cobalt led to an increase in the aging effect. Titanium and aluminum, in turn, also influenced the aging process in the future. M.A. Cerra Flore, Ú.C. Pereira, J.L. Cardoso, F.J. Santos Oliveira, W.S. Araújo, G.F. Ribas, H.F. Gomesde Abreu & M.J. Gomes da Silva [12] obtained results indicating a decrease in the electrochemical corrosion resistance of maraging steels in relation to the amount of content of certain elements. The dissolution of alloying elements in iron occurs due to the replacement of Fe atoms by impurity atoms. Changing the dimensions of the α-lattice leads to a change in properties, i.e., morphology mainly depends on the chemical composition. For example, doping with substances such as Mo, Ti and Ni can increase the density. The content of Ni and Ti is necessary for the formation of intermetallic phases that cause aging. The presence of a high content of Ni, Si, or Mn compared to Cr, Mo, and W strengthens the single-phase region γ to room temperature, i.e., contributes to martensitic transformation, which hardens the steel. Ni stabilizes the γ-solid solution, while reducing the transformation temperature $\gamma \rightarrow \alpha$. The addition of refractory Re to the overall chemical composition can increase the hardness after heat treatment. In turn, Re has the ability to reduce the self-diffusion coefficient, which mainly leads to high thermal stability [13]. For example, in the paper of A. Fedoseeva, I. Nikitin & N. Dudova [14; 15], Re was added to the martensitic steel and the results show that this hardened the steel. At that, the presence of Ti negatively affects the processibility of the alloy. Re also gives the microstructure a hierarchical appearance, which consists of austenite grains in the form of blocks with martensite laths. The absence of Ti leads to the absence of precipitates, more specifically, the nickel-based intermetallic compound of the Ni_3Ti type, which, in turn, is the main hardening precipitate and dissolves in the γ'-phase [16; 17].

S. Dehgahi, H. Pirgazi, M. Sanjari, R. Alaghmandfard, J. Tallon, A. Odeshi, L. Kestens, M. Mohammadi, M.H. Ghoncheh & B. Shalchi Amirkhiz [18; 19] reported an increase in the proportion of the austenite phase after heat treatment by increasing Ti, where it promotes the formation of austenite in the presence of Ni and Mo. The presence of titanium (TiO_2) or molybdenum (MoO_3) oxides gives the steel additional protection. It has also been found that ductility was improved in samples with a high Ti content by developing the copper texture and fibers that facilitate the movement of dislocations. The reversible kinetics of γ formation, stimulated by the addition of Ti, has the greatest strengthening effect due to Ni_3Ti precipitates in the matrix. J. Tian, W. Wang, H. Li, K. Yang, Z. Jiang [20] demonstrated that specimens with a high titanium content are more ductile but have lower strength compared to specimens with a low Ti content. J. Tian, W. Wang, H. Li, K. Yang, Z. Jiang [20] investigated martensitic steels with different Ti content. From the analysis results, it can be noted that the martensite content is almost the same in various powder mixtures. The addition of Co in the presence of Mo in the alloying elements reduces the solubility limit in the lattice coordinate system, contributing to the formation of a uniform volume fraction of the Fe_2Mo precipitates dispersion.

S. Dehgahi, M.H. Ghoncheh, A. Hadadzadeh, M. Sanjari, B. Shalchi Amirkhiz & M. Mohammadi [21] confirmed the presence of CoNi precipitates and a high fraction of dislocations in horizontal samples with a large amount of Ti, which implies good strength of the samples. It is also worth paying attention to raising questions about the hardening of maraging alloys by copper deposition. At the initial stage of the process, Cu is deposited as a precipitate with a body-centered lattice in the α-Fe matrix, maintaining the integrity of the structure up to the peak quenching temperature. For example, G. Yang, F., Deng, S. Zhou, B. Wu & L. Qin [22] developed a new maraging steel reinforced with copper. The results show that the microstructure of such steel is mainly composed of lath martensite, δ-ferrite, as well as reduced austenite in the precipitated state. After quenching and direct aging, the microstructure consisted of martensite and reduced austenite. But it is worth noting that copper does not form compounds with iron and its solubility is about 1%. Maraging alloy steels have excellent stress resistance and corrosion resistance. However, the high cost of alloying additions such as Co or Mo prevents their widespread use [5]. In this connection, a recent promising direction is the development of maraging steels without the addition of Co, while preserving good characteristics. The addition of a large amount of Cr to improve corrosion resistance may cause the formation of precipitates, which will lead to brittleness, more precisely, the cold brittleness threshold will increase [23]. Therefore, the development of ultra-strong maraging steels with good ductility, stability and economic benefits is of great interest.

Powder metallurgy has recently gained momentum as a promising technology for the production of steels due to the production of steels with a homogeneous microstructure, which gives it the expected characteristics. The current technology used for powder steels is spark plasma sintering (SPS), which was applied to obtain these samples. This sintering technology pays attention to the rapid compaction of the powder mixture to a high density (up to 95% for the presented samples) at low temperature ranges, but at a fast time interval (in this case in 180 s) compared to traditional sintering methods. In the manufacture of steel using the SPS method, the sample is subjected to rapid sintering and then cooling, which removes nitrogen well and gives greater performance and high density. However, it must also be taken into account that the morphology and size of the powder affects the density of sintering. More precisely, the smaller the size of the powder, the denser it is sintered. During SPS sintering, plastic deformation occurs, i.e., the throughput of a pulsed direct current through the sample forms an electric field. It is also important that the powder is heated inside and outside and melted by applying pressure, which has a good effect on the sintering density and functional characteristics of the sample. The sintering temperature in this way can reach up to 2500°C, resulting in high-quality steel [24]. The preparation of maraging steels using the SPS method will not allow abrasive phases and side reactions to occur. For example, these samples were also tested for abrasion resistance, the results of which are shown in Figure 7. According to the experimental values obtained, it is noticeable that the abrasion resistance is much higher than that of other steels. This technology also has low cost (saving up to 80%), which is an important criterion.

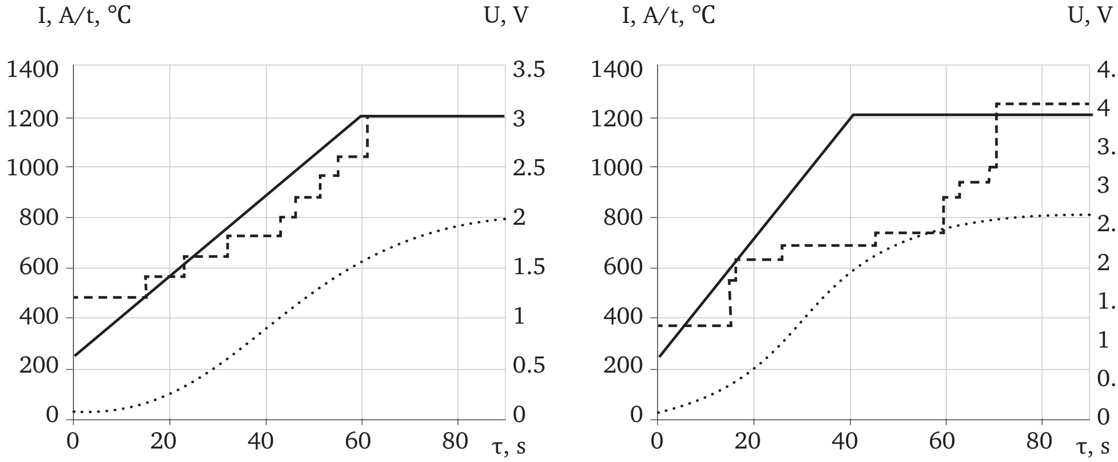

Figure 7. Experimental data results

Note: *1 – current strength; 2 – voltage; 3 – temperature in time during spark plasma sintering of the mixture 18%Ni+9%Co+5%Mo+1%Ti+1%Re+66%Fe at different heating rates*
Source: [25]

Recently, the method of additive manufacturing has gaining popularity, namely, the production of powder steel using laser deposition. Materials made using this technology demonstrate really good results, namely the unique microstructure and defects that can be controlled to obtain effective mechanical characteristics. For example, M.J. Paul, Y. Muniandy, J.J. Kruzica, U. Ramamurty & B. Gludovatz [26], Zh. Zhao, L. Wang, D. Konga, P. Liu, X. He, X. Ni, L. Zhang, Ch. Dong [27] and D. de Baere, M. Moshiri, L. Smolej & J.H. Hattel [28] obtained a maraging powder steel, the samples of which had high hardness, which allows increasing the development and use period. Maraging steels harden according to the general law of metals with a body-centered lattice, which favorably affects such characteristics as hardness, yield stress and strength. At that, to obtain the expected values, it is necessary should monitor the substance's structure. As mentioned above, powder mixture laser deposition technology is widely used, in which a metal powder mixture is developed by laser beam assimilation one layer after another upon solidification. Obtaining optimal hardness with the help of LB-PBF (laser beam-powder bed fusion) technology requires improvements, i.e., carrying out hardening or aging. Thus, carrying out heat treatment during the laser processing will give the expected results, thus neglecting post-thermal processing.

N. Nouri, Q. Li, J. Damon, F. Mühl, G. Graf, S. Dietrich & V. Schulze [29] developed a new maraging steel by the LB-PBF method. The results show a reduction in time and cost for optimizing steel characteristics. It should be noted that the crystallographic texture also depends on the strain rate and other laser processing parameters. For example, S. Dehghahi, H. Pirgazi, M. Sanjari, R. Alaghmandfard, J. Tallon, A. Odeshi, L. Kestens, M. Mohammadi, M.H. Ghoncheh & B. Shalchi Amirkhiz [18; 19] addressed this issue, showing that the strain rate does not have a significant effect on the texture in samples that have undergone heat treatment. The results of the paper by M.A. Cerra Flore, Ú.C. Pereira, J.L. Cardoso, F.J. Santos Oliveira, W.S. Araújo, G.F. Ribas, H.F. Gomesde Abreu & M.J. Gomes da Silva [12] show that quenching has a significant effect in terms of transformation and variability in the microstructure of the sample. At that, proper selection of heat treatment parameters can eliminate microstructure defects. The microstructure of steels produced by laser processing consists of martensite with precipitates and preserved austenite. However, L. Guo, L. Zhang, J. Andersson & O. Ojo [30] report that the content of precipitates can reduce ductility and fracture toughness. Thus, the production of powder steel using the LB-PBF technology results in samples with favorable characteristics. The microstructures of such steels can reach high hardness values compared to conventional samples produced by traditional methods. Research shows that this technology also allows achieving an age hardening effect. Heat treatment during the production process can potentially lead to sufficient age hardening to allow post-heat treatment to be neglected. In the manufacture of steels by this technology, each layer of material is subjected to a repeated heating cycle, which leads to repeated austenization and the nucleation of martensite. It is also worth noting that the microstructure of steels produced by laser processing consists of martensite with precipitates and preserved austenite. A typical structure of steel produced by laser processing can be described as follows:

– the formation of multilevel hierarchical solidification systems such as molten precipitate boundaries, columnar or equiaxed grain boundaries, as well as ultrathin subgrain boundaries (i.e., columnar, dendritic and cellular subgrains);

– the distribution of segregation of elements and retained austenite along the subgrain boundaries.

Plasma nitriding has also proven itself as an effective and innovative method for improving the surface quality of maraging steel. The thermal effect of the nitriding reaction, in which energy is released or absorbed, leads to hardening of the maraging steel. Theoretically, the mechanical properties of laser-produced steel can be improved through the effect of simultaneously undergoing the aging and nitriding process. Y Hong, D.D. Dong, S.S. Lin, W. Wang, C.M. Tang, T.C. Kuang, M.J. Dai [31] report an improvement in the hardness and wear resistance of maraging steel by performing plasma nitriding, during which a nitrided layer is formed.

Conclusions

The studied powder steel grade PS-H18K9M5TR, pressed by spark plasma sintering, is a heavy-duty maraging steel, the hardness value of which amounts to 60 HRC according to the Rockwell method. The presence of a number of alloying elements such as cobalt, molybdenum, titanium and rhenium gives this steel an advantage over other structural materials. After quenching, a uniform distribution of finely dispersed particles of secondary phases takes place in the martensitic matrix. In the course of the research, elemental and phase analyzes were carried out, microphotographs of the structure were obtained and described. In the course of elemental analysis, regions enriched in iron were identified; the basis of the compressed powder mixture is an iron frame. Elemental analysis also shows that there is a large amount of iron on the surface with added alloying elements within the range above 26 microns.

The high content of Ni promoted martensitic transformation, increased the strength of the steel without reducing toughness, as well as reduced the cold brittleness threshold, thereby reducing the likelihood of brittle fracture. During phase analysis, it was noticed that diffusion reactions slowdown, which in turn affects the formation of phase inhomogeneity throughout the volume of the material obtained, or rather, the presence of precipitates. The high Ti content resulted in improved strength due to martensitic phase transformation and precipitation hardening. The presence of Re in the studied grade gives the steel a special advantage – a low diffusion rate, which fundamentally affects the thermal stability. This, in turn, increases the operating range of the final material, which helped to form a further study of the effect of the content of Ti, Re and precipitates on the structure, as well as physical and mechanical functional characteristics of steel.

New technologies for the manufacture of powder steels lead to improved optimization of maraging steels, i.e., there is an improvement in the chemical composition with properties superior to those of traditional steels. There is a spread of maraging steel powder in the laser additive production, because its low carbon content helps prevent thermal cracking on cooling. In addition, the parts produced in this way have high strength and hardness. Powder mixture laser sintering (LB-PBF) is a method, by which a sample of the same mixture is to be examined and compared with the spark plasma sintering method. The sintering parameters of the powder mixture in both methods significant affect the microstructure, morphological features and functional qualities of maraging steels, from which the next task is set for further research.

References

[1] Leibova NM, Zoteva AS, Kagan ES, Felikson AE. Use of maraging steels for parts of metal working machines. *Met. Sc. and H. Treat.* 1974;(16):852-55.

[2] Rusanenko VV, Zhukov OP, Blinova EN, Filippova VP, Makuschev SYu. Structure and properties of high-strength iron-nickel maraging steels. *B. of the Rus. Acad. of Sc.: Phys.* 2012;(76):1217-20.

[3] van Swam LF, Pelloux RM, Grant NJ. Fatigue behavior of maraging steel 300. *Metallur. Transac.* 1975;(6):45-54.

[4] Chernyshova TA, Lyulkina TV. Influence of rapid quenching of the melt on structure and properties of maraging steel. *J. of Mater. Sc.* 1992;(27):580-86.

[5] Hu Z-F, Wang Ch-Xu. Effect of tube spinning with subsequent heat-treatment on performance and microstructure evolution of T250 Maraging Steel. *Internat. J. of Ir. and St. Resear.* 2012;(19(5)):63-68.

[6] Pardal JM, Tavares SSM, Terra VF, da Silva MR, dos Santos DR. Modeling of precipitation hardening during the aging and overaging of 18Ni–Co–Mo–Ti maraging 300 steel. *J. of Al. and Comp.* 2005;(393(1-2)):109-13.

[7] Grachev SV, Shein AS. High-strength maraging steels. *Met. Sc. and Heat Treatm.* 1989;(31):237-43.

[8] Morris JWJr. Making steel strong and cheap. *Nat. Mater.* 2017;(16):787-89.

[9] Li H, Liu Y, Liu B, Wei D. Synergistic enhancement of strength and ductility of cobalt-free maraging steel via nanometer-scaled microstructures. *Mater. Sc. and Engineer.* 2022;(842):article number 143099.

[10] Manohar G, Pandey KM, Maity SR. Effect of spark plasma sintering on microstructure and mechanical properties of AA7075/BC/ZrC hybrid nanocomposite fabricated by powder metallurgy techniques. *Mater. Chem. and Phys.* 2022;(282):article number 126000.

[11] Tian J, Wang W, Li H, Babar Shahzad M, Shan Y, Jiang Zh, et al. Effect of deformation on precipitation hardening behavior of a maraging steel in the aging process. *Mater. Character.* 2019;(155):article number 109827.

[12] Cerra Florez MA, Pereira ÚC, Cardoso JL, Santos Oliveira FJ, Araújo WS, Ribas GF, et al. Microstructural characterization of grade 300 and grade 350 maraging steels and electrochemical study in hydrofluoric solution. *J. of Fluor. Chem.* 2021;(243):article number 109738.

[13] Kablov EN, Petrushin NV, Bronfin MB, Alekseev AA. Features of single-crystal heat-resistant nickel alloys alloyed with rhenium. *Metals*. 2006;(5):1-24.

[14] Fedoseeva A, Nikitin I, Dudova N. Selection of heat treatment regime for advanced heat-resistant 10%Cr-3%Co-3%W-0.2%Re martensitic steel. *Tam. Univer. Rep.* 2018;(23(122)):298-02.

[15] Fedoseeva A, Nikitin I, Dudova N, Kaibyshev R. On effect of rhenium on mechanical properties of a high-Cr creep-resistant steel. *Mater. Let.*, 2018;(236):81-84.

[16] Rangasayee K, Donovan NL, Peeyush N. Optimization of direct aging temperature of Ti free grade 300 maraging steel manufactured using laser powder bed fusion (LPBF). *Mater. Sc. and Engineer.* 2021;(817):article number 141266.

[17] Kablov EN. Physico-chemical and technological features of the creation of heat-resistant alloys containing rhenium. *B. of the Mos. Univer.*2005;(46(3)):155-167.

[18] Dehgahi S, Pirgazi H, Sanjari M, Alaghmandfard R, Tallon J, Odeshi A, Kestens L, Mohammadi M. Texture evolution during high strain-rate compressive loading of maraging steels produced by laser powder bed fusion. *Mater. Character.* 2021;(178):article number 111266.

[19] Dehgahi S, Sanjari M, Ghoncheh MH, Shalchi Amirkhiz B, Mohammadi M. Concurrent improvement of strength and ductility in heat-treated C300 maraging steels produced by laser powder bed fusion technique. *Addit. Manufact*. 2021;(39):article number 101847.

[20] Tian J, Wang W, Li H, Yang K, Jiang Z. Understanding main factors controlling high cycle fatigue crack initiation and propagation of high strength maraging stainless steels with Ti addition. *Mater. Sc. and Engineer.* 2021;(805):article number 140589.

[21] Dehgahi S, Ghoncheh MH, Hadadzadeh A, Sanjari M, Shalchi Amirkhiz B, Mohammadi M. The role of titanium on the microstructure and mechanical properties of additively manufactured C300 maraging steels. *Mater. & Des.*2020;(194):article number 108965.

[22] Yang G, Deng F, Zhou S, Wu B, Qin L. Microstructure and mechanical properties of a novel Cu-reinforced maraging steel for wire arc additive manufacturing. *Mater. Sc. and Engineer.* 2021;(825):article number 141894.

[23] Wang ZH, Niu B, Wang Q, Dong C, Jie JC, Wang TM, et al. Designing ultrastrong maraging stainless steels with improved uniform plastic strain via controlled precipitation of coherent nanoparticles. *J. of Mater. Sc. & Technol.*2021;(93):60-70.

[24] Mahale RSh, Shamanth V, Sharath PC, Shashanka R, Hemanth K. A review on spark plasma sintering of duplex stainless steels. *Materialst. Proceed.* 2021;(45(1)):138-44.

[25] Simonyan VA. Research of maraging steels powder blend fussing and compression. *Techn. Sc*. 2022;(5(119)):102-07.

[26] Paul MJ, Muniandy Y, Kruzica JJ, Ramamurty U, Gludovatz B. Effect of heat treatment on the strength and fracture resistance of a laser powder bed fusion-processed 18Ni-300 maraging steel. *Mater. Sc. and Engineer.* 2022;(844):article number 143167.

[27] Zhao Zh, Wang L, Konga D, Liu P, He X, Ni X, et al. Texture dependence on the mechanical properties of 18Ni300 maraging steel fabricated by laser powder bed fusion. *Mater. Character.* 2022;(189):article number 111938.

[28] de Baere D, Moshiri M, Smolej L, Hattel JH. Numerical investigation into laser-based powder bed fusion of cantilevers produced in 300-grade maraging steel. *Addit. Manuf.* 2022;(50):article number 102560.

[29] Nouri N, Li Q, Damon J, Mühl F, Graf G, Dietrich S, et al. Characterization of a novel maraging steel for laser-based powder bed fusion: Optimization of process parameters and post heat treatments. *J. of Mater. Resear. and Technol.* 2022;(18):931-42.

[30] Guo L, Zhang L, Andersson J, Ojo O. Additive manufacturing of 18% nickel maraging steels: Defect, structure and mechanical properties. *J. of Mater. Sc. & Technol.* 2022;(120):227-52.

[31] Hong Y, Dong DD, Lin SS, Wang W, Tang CM, Kuang TC, et al. Improving surface mechanical properties of the selective laser melted 18Ni300 maraging steel via plasma nitriding. *Surf. and Coat. Technol.* 2021;(406):article number 126675.

Дослідження зміцнення та структури мартенситно-порошкової сталі марки PS-H18K9M5TR (18%Ni+9%Co+5%Mo+1%Ti+1%Re+66%Fe)

Сурен Агбалян[1], Віген Симонян[2]

[1]Доктор технічних наук, профессор. ORCID: https://orcid.org/0000-0001-9987-8515.
Національний політехнічний університет Вірменії,
0009, вул. Терян, 105, м. Єреван, Республіка Вірменія

[2]аспірант. ORCID: https://orcid.org/0000-0002-9293-0955.
Національний політехнічний університет Вірменії,
0009, вул. Терян, 105, м. Єреван, Республіка Вірменія

Анотація

Актуальність. Високоміцні сталі користуються все більшим попитом у сучасній промисловості для різних застосувань. Мартензитно-старінні сталі є основним матеріалом для виготовлення більшості деталей літаків, а також компонентів машинобудування. Цей тип є низьковуглецевим і багатий нікелем, який утворює мартенсит при охолодженні, а також демонструє такі властивості, як висока твердість, зносостійкість тощо. Процес гартування є основним фактором, що впливає на функціональні властивості мартенситно-старої сталі. При певних температурах аустеніт має здатність переходити в різного роду фази. Однак недолік, який полягає в наявності деяких домішок, обмежує встановлені типи технологій поліпшення, що призводить до пошуку інноваційних методів поліпшення характеристик сталі без втрати будь-яких бажаних властивостей. Хороші якості з'являються в мартенситно-стартових сталях в основному після обробки розчином при температурі близько 1000°C і під час старіння при температурі близько 490°C.

Мета. Отже, метою цієї наукової роботи є аналіз структури порошків мартенситно-стартової сталі та вивчення термічного впливу на її властивості.

Методологія. У цій роботі порошкову сталь пресували за технологією іскрового плазмового спікання під тиском 60 МПа до порошкової компактної форми та нагрівали при температурі 1100°C протягом 180 с зі швидкістю 20°C/с, після чого зразки піддавалися фазі та елементного аналізу було виміряно їх твердість, значення якої склало близько 60 HRC.

Результати. Результати цього наукового дослідження демонструють наявність різноманітних опадів. Наявність таких домішок, як Co, Ti, Re призводила до підвищення міцності за рахунок мартенситного фазового перетворення та дисперсійного зміцнення, а також уповільнювала процес дифузії.

Висновки. Крім того, визначено завдання для подальших досліджень з проблеми виготовлення мартенситностартових сталей адитивним методом виробництва. Ця технологія дозволяє отримувати міцні мартенситно-стареючі сталі на основі порошкової суміші з необхідними характеристиками

Ключові слова: іскрове плазмове спікання, лазерна обробка, адитивне виробництво, надміцна сталь, термічна обробка

НАУКОВИЙ ВІСНИК
УЖГОРОДСЬКОГО УНІВЕРСИТЕТУ
СЕРІЯ «ФІЗИКА»

Науковий журнал

Випуск 52. 2022

Заснований у 1997 р. Виходить двічі на рік

Оригінал-макет видання виготовлено
у редакційно-видавничому відділі Ужгородського національного університету

Відповідальний редактор:
Г. Івченко

Редагування англомовних текстів:
С. Воровський, К. Касьянов

Комп'ютерна верстка:
К. Сосєдко

Підписано до друку 22.12.2022 р. Формат 60*84/8
Умовн. друк. арк. 6,6
Наклад 300 примірників

Адреса видавництва:
ДВНЗ «Ужгородський національний університет»
88000, вул. Університетська, 54, м. Ужгород
Закарпатська область, Україна
тел/факс: (03122) 3-20-24
E-mail: info@physics.uz.ua
www: https://physics.uz.ua/uk

SCIENTIFIC HERALD
OF UZHHOROD UNIVERSITY
SERIES "PHYSICS"

Scientific Journal

Issue 52. 2022

Founded in 1997. Published two times per year

The original layout of the publication is made
in the publishing department of Uzhhorod National University

Managing editor:
H. Ivchenko

Editing English-language texts:
S. Vorovsky, K. Kasianov

Desktop publishing:
K. Sosiedko

Signed for print 12/22/2022. Format 60*84/8
Conventional printed pages 6.6
Circulation 300 copies

Publishing Address:
Uzhhorod National University
88000, 14 Universytetska Str., Uzhhorod
Transcarpathian region, Ukraine
Tel./fax: (03122) 3-20-24
E-mail: info@physics.uz.ua
www: https://physics.uz.ua/en